Mechanics of Advanced Materials and Structures

ISSN: 1537-6494 (Print) 1537-6532 (Online) Journal homepage: www.tandfonline.com/journals/umcm20

Integration of three-beam laser interference lithography and metal assisted chemical etching for enhanced electrical and antireflection characteristics in Si micro/nano structures

Sadaf Saeed, Ali Zia, Umema Shakoor, Kinza Arshad, Sana Tariq, Changrui Liao & Zuobin Wang

To cite this article: Sadaf Saeed, Ali Zia, Umema Shakoor, Kinza Arshad, Sana Tariq, Changrui Liao & Zuobin Wang (06 Mar 2025): Integration of three-beam laser interference lithography and metal assisted chemical etching for enhanced electrical and antireflection characteristics in Si micro/nano structures, Mechanics of Advanced Materials and Structures, DOI: 10.1080/15376494.2025.2468379

To link to this article: https://doi.org/10.1080/15376494.2025.2468379

MECHANICS OF ADVANCED MATERIALS AND STRUCTURES
https://doi.org/10.1080/15376494.2025.2468379

Taylor & Francis
Taylor & Francis Group

ORIGINAL ARTICLE

Integration of three-beam laser interference lithography and metal assisted chemical etching for enhanced electrical and antireflection characteristics in Si micro/nano structures

Sadaf Saeed[a,b,c,d,e], Ali Zia[f], Umema Shakoor[g], Kinza Arshad[h], Sana Tariq[i], Changrui Liao[a,b,c,d]*, and Zuobin Wang[e]*

[a]Shenzhen Key Laboratory of Ultrafast Laser Micro/Nano Manufacturing, College of Physics and Optoelectronic Engineering, Shenzhen University, Shenzhen, China; [b]Key Laboratory of Optoelectronic Devices and Systems of Ministry of Education/Guangdong Province, College of Physics and Optoelectronic Engineering, Shenzhen University, Shenzhen, China; [c]Shenzhen Key Laboratory of Photonic Devices and Sensing Systems for Internet of Things, Guangdong and Hong Kong Joint Research Centre for Optical Fibre Sensors, Shenzhen University, Shenzhen, China; [d]State Key Laboratory of Radio Frequency Heterogeneous Integration, Shenzhen University, Shenzhen, China; [e]Centre for Opto/Bio-Nano Measurement and Manufacturing, Zhongshan Institute of Changchun University of Science and Technology, Zhongshan, China; [f]School of Physics and Optoelectronic Engineering, Beijing University of Technology, Beijing, China; [g]Materials Simulation Research Laboratory (MSRL), Institute of Physics, Bahauddin Zakariya University, Multan, Pakistan; [h]Microsystem and SemiConductor Technology Lab, Shenzhen University, Shenzhen, China; [i]State Key Laboratory of Applied Optics, Changchun Institute of Optics, Fine Mechanics and Physics, Chinese Academy of Sciences, Changchun, China

ABSTRACT

The integration of three-beam laser interference lithography (TBLIL) and Metal-Assisted Chemical Etching (MACE) is a novel approach to enhance the electrical and antireflection properties of silicon micro/nanostructures (SiMNs) for advanced optoelectronic applications. This study explored the fabrication, theoretical modeling, and performance evaluation of SiMNs with enhanced light absorption, electrical conductivity, and reduced surface reflectance. A three-dimensional finite-difference time-domain (FDTD) method was employed to simulate and optimize the surface texture design for improved light absorption. The electrical and optical characteristics of the fabricated SiMNs were thoroughly examined. The simulated and experimental results exhibited comparable trends. The integration of TBLIL and MACE not only offers a precise and scalable method for structuring SiMNs, but also provides valuable insights for the development of high-efficiency optoelectronic devices, positioning these arrays as promising candidates for next-generation technologies.

GRAPHICAL ABSTRACT

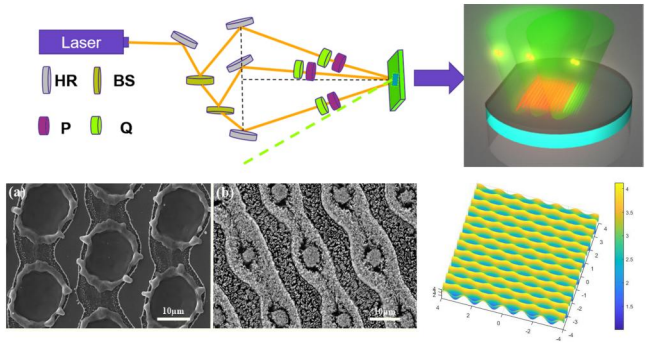

ARTICLE HISTORY
Received 17 November 2024
Accepted 13 February 2025

KEYWORDS
Three-beam laser interference lithography; metal-assisted chemical etching; electrical properties; silicon microstructures; antireflection

1. Introduction

Researchers have focused on semiconductor silicon micro-and nanostructures (SiMNs) for decades owing to their outstanding electronic and photonic capabilities [1–4]. SiMNs have attracted considerable interest owing to their superior electrical, optical, and mechanical properties. These features include a high surface-to-volume ratio, exceptional electrical conductivity, and configurable bandgap, making them excellent candidates for a wide range of applications, including solar cells [5], sensors [6], photodetectors, and optoelectronic devices [7–10]. The

CONTACT Sadaf Saeed sadafsaeed@szu.edu.cn; cliao@szu.edu.cn; wangz@cust.edu.cn College of Physics and Optoelectronic Engineering, Shenzhen University, Guangdong Province, Shenzhen 518060, China.
*Supervisory role.

Supplemental materials are available for this article at https://doi.org/10.1080/15376494.2025.2468379

performance of these devices depends on two critical characteristics, namely, high electrical conductivity and minimal light reflectance. To achieve these properties, researchers have explored various structuring and surface treatment methods. However, combining electrical and optical enhancements in a single scalable fabrication process remains challenging [11–14]. Among various approaches, Nano structuring Si surfaces has shown great promise in overcoming these challenges, particularly in improving light absorption and reducing surface reflection [15–21]. Because of their high intrinsic reflectivity, surface engineering approaches, such as antireflective coatings (ARCs) [22] or surface micro/nanostructuring [23], are essential for high-performance architectures. ARCs can provide a straightforward way to reduce surface reflection losses and angular reflectivity dependence, which affect photovoltaic systems, display contrast, and brightness [24]. To achieve wideband anti-reflectance, an ARC must carefully choose materials with specified refractive indices and precisely calibrate layer thicknesses [25].

Microstructures and nanostructures have been fabricated using several patterning techniques, such as photolithography [26,27], nanoimprinting [28], nanosphere lithography [29], and colloidal lithography [30]. These strategies were used to produce periodic structures [31,32]. However, most of these methods require complex and costly lithographic masks, high experimental temperatures, high costs, and long fabrication times, owing to the limitations of the growth mechanisms. Furthermore, it is difficult to create large aspect ratios to adjust and obtain the structures of the different parameters according to the specific wavelength. Compared with other approaches for producing surface micro/nanostructures, metal-assisted chemical etching (MACE) is a simpler and more controllable approach that does not require specialized equipment or complex techniques. Furthermore, chemical etching is particularly suited for the creation of large-scale surface micro/nanostructures, which can be precisely controlled by altering their composition, concentration, or temperature [33,34].

The benefits of lithography for creating surface micro/nanostructures include high controllability of the prepared micro/nanostructures, such as controlling the shape and size of the structures through factors such as the exposure agent type and exposure duration [35–37]. Saeed et al. [38] explored broad-band antireflection structures with gold micropatterns by laser interference lithography. Lee et al. [37] explored antireflection silicon structures with hydrophobic properties fabricated by three-beam laser Interference lithography. Senthuran et al. [39] reported a maskless and scalable technique for fabricating nanoscale inverted pyramid structures suitable for light management in crystalline Si solar cells. Zhang et al. [36] fabricated periodic antireflection structures with an average reflectance of 3.5% on silicon using four-beam laser interference lithography. Wang et al. [40] proposed both antireflection and superhydrophobicity structures fabricated by direct laser interference nanomanufacturing. Li et al. [41] presented a method for the fabrication of highly-ordered superhydrophobic micro-nano dual structures on silicon by direct laser interference lithography. The antireflection and self-cleaning functions were due to the formation of an array of micro cone and hole structures [42] on the silicon wafer surfaces. Three-beam laser interference lithography (TBLIL) allows rapid, low-cost patterning over large areas, making it possible to produce periodic structures with flexible designs and wavelength adaptability. When followed by MACE, which uses a metal catalyst to etch silicon selectively, this combination achieves high aspect ratios without high temperatures or extended synthesis times, which is typical for other methods. This two-step approach is versatile, efficient, and cost-effective and provides a scalable and adaptable method for creating SiMNs with precise dimensions tailored to specific applications. Furthermore, the nanostructuring process also advances beneficial modifications to the Si surface, enhancing its electrical properties, such as reduced carrier recombination rates and improved charge carrier mobility [38].

This article presents an integrated approach combining TBLIL and MACE to fabricate SiMNs with superior antireflection and electrical properties. In this study, we fabricated and characterized SiMN arrays with controlled morphology, power, and energy using TBLIL combined with MACE. We present MATLAB and FDTD simulations and laser-based fabrication approaches for the antireflection and conductivity mechanisms. This technique has two primary purposes. The first was to create periodic sub-nanostructures in the Si wafers, and the second was to investigate the effect of this patterning on the reflectance and conductivity of the nanostructures. Integrating these two techniques opens new avenues for developing high-efficiency Si-based devices, potentially contributing to the advancement of renewable energy technologies and the broader field of nanotechnology.

2. Materials and methods

Single-sided Si wafers (P-type, 10 Ω cm, 500 μm thickness with (100) alignment) were set up to 2 cm^2 as the samples. The Si substrates were then cleaned with acetone (CH_3COCH_3, 99% purity) and ethanol (CH_3CH_2OH, 99% purity) for 10 min and rinsed multiple times with deionized water. Ag was deposited using a JFC-1600 ion sputter coater (Quorum Technologies Q150T) on 20-, 30-, 35-, 40-, 45-, and 50 nm thick substrates. After deposition, a TBLIL (German INNOLAS Spit Light 2000) high-power Nd: YAG laser source with a wavelength of 1064 nm, frequency of 10 Hz, laser pulse energy of 40–50 $mJcm^{-2}$, pulse width of 7–9 ns, voltage of 560, 580, and 600 V, laser beam spot size of 6 mm, and exposure time of 10s was struck on the samples. Initially, the laser beam was dispersed into three beams with incident angles of 5.5°, 30°, and 45° and azimuthal angles $\varphi_1 = 0°$, $\varphi_2 = 120°$, and $\varphi_3 = 240°$. The polarization of the TE-TE-TE, TE-TE-TM, and polarizers were $P_1 = P_2 = P_3 = 90°$. They were then recombined on the surfaces of the substrates to create periodic patterns.

Figures 1 and 2 show experimental schematic diagrams of the SiMNs. Figure 1 shows the three-beam LIL setup and computer simulation results. Three laser beams were obtained using beam splitters (BS). The beams can be varied

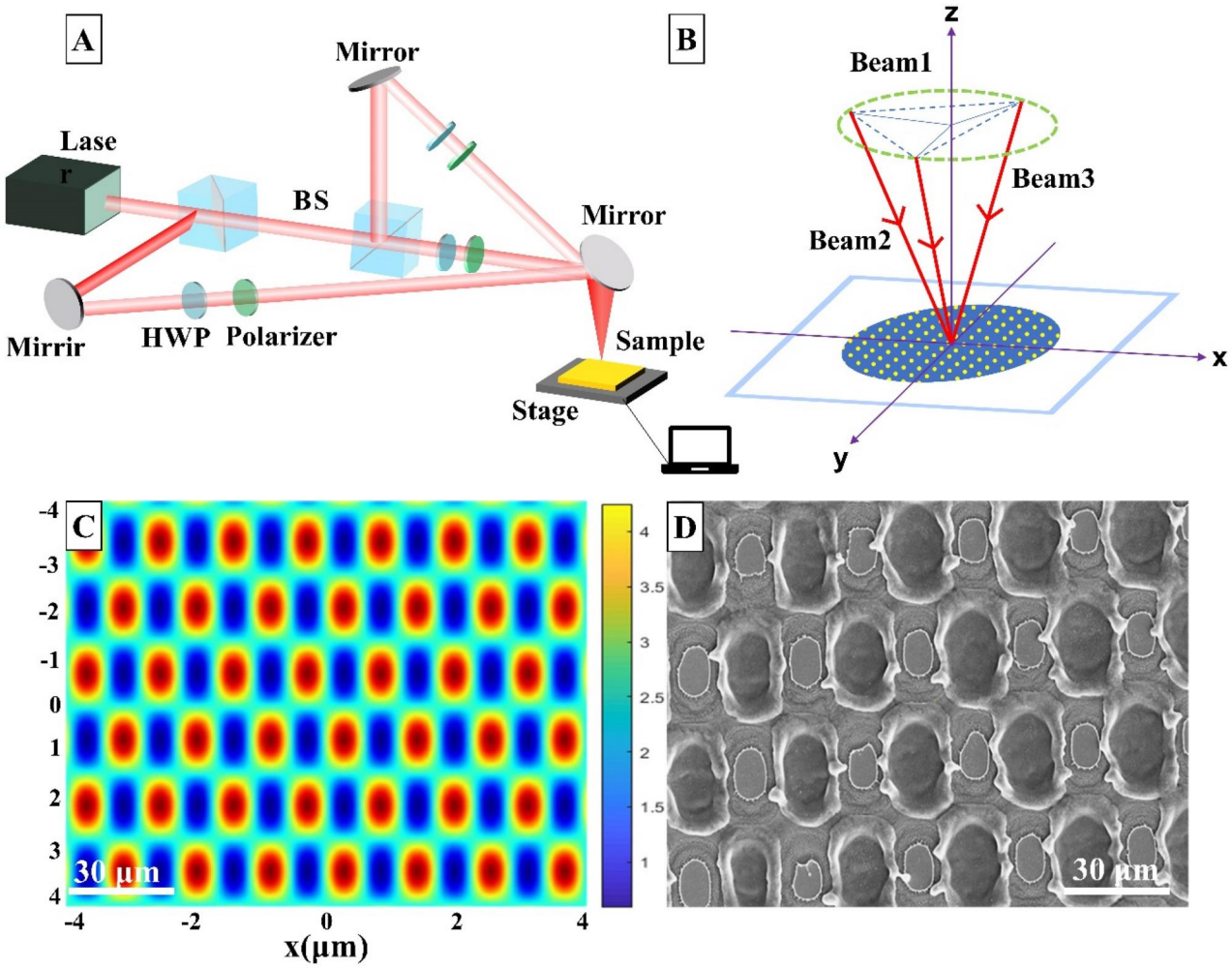

Figure 1. (A) Schematic of the experimental setup for the TBLIL. The setup included a laser source, beam splitters (BS), a half-wave plate (HWP), a polarizer, mirrors, and a stage for the sample. (B) Illustration of a three-beam interference pattern formed at the sample surface, showing beams arranged to create a periodic interference pattern in the x-y plane. (C) Simulation of the interference pattern displaying a periodic array with controlled dimensions for the SiMN fabrication. (D) Scanning electron microscopy (SEM) images of the SiMNs fabricated at 30 μm.

by controlling the positions of the highly reflective mirrors (HR). The polarization directions and output energies were determined using 1/4-wave plates (Q) and polarizers (P). The computer simulation results showed the intensity distribution of the interference pattern, as shown in Figure 1(C). The red and blue areas indicate the high and low intensities, respectively. The image shows the periodic interference pattern produced by the three-beam interference setup illustrated in Figure 1(A,B). The bright and dark regions in the simulated pattern correspond to the areas of constructive and destructive interference, respectively. These periodic regions provide a template for creating structures with controlled dimensions, allowing precise patterning at the micro- and nano-scales.

Figure 2 shows a schematic illustration of the MATLAB simulation and fabrication mechanism of the SiMN arrays. Figure 2(A) shows the sequential steps involved in creating SiMNs. In Figure 2(A), colors are used to distinguish the various stages and components involved in the fabrication process of the SiMNs. The blue color represents the Si substrate, which served as the foundation for the entire process. Initially, the Si wafer was prepared and cleaned to ensure a smooth surface for the subsequent steps. Subsequently, Ag was deposited onto the Si substrate. The gray color indicates the Ag layer deposited on top of the Si substrate. This Ag layer plays a critical role in the fabrication process by acting as a catalyst during the wet chemical etching phase. After the deposition, the substrate with the Ag layer was exposed to a high-power laser through a TBLIL. Following laser exposure, the samples underwent wet chemical etching using a solution of hydrofluoric acid (HF), hydrogen peroxide (H_2O_2), and deionized water. The etching solution was prepared in an etch bath containing HF, deionized water, and H_2O_2 as shown in Figure 2(B). The concentrations of deionized water, H_2O_2, and HF were 37.5, 1.5, and 15 mL, respectively. After preparing the solution, the substrates were dropped into the solution for approximately 40–50 min. [43]. The yellow color highlights the regions in Figure 2(A) where wet chemical etching occurs, specifically beneath the metal nanoparticles. The color scheme differentiates between the Si substrate, metal layer, and areas where specific reactions occur during the fabrication process, making the steps and their interactions clearer to the viewer. The final step involved removing the metal, leaving behind

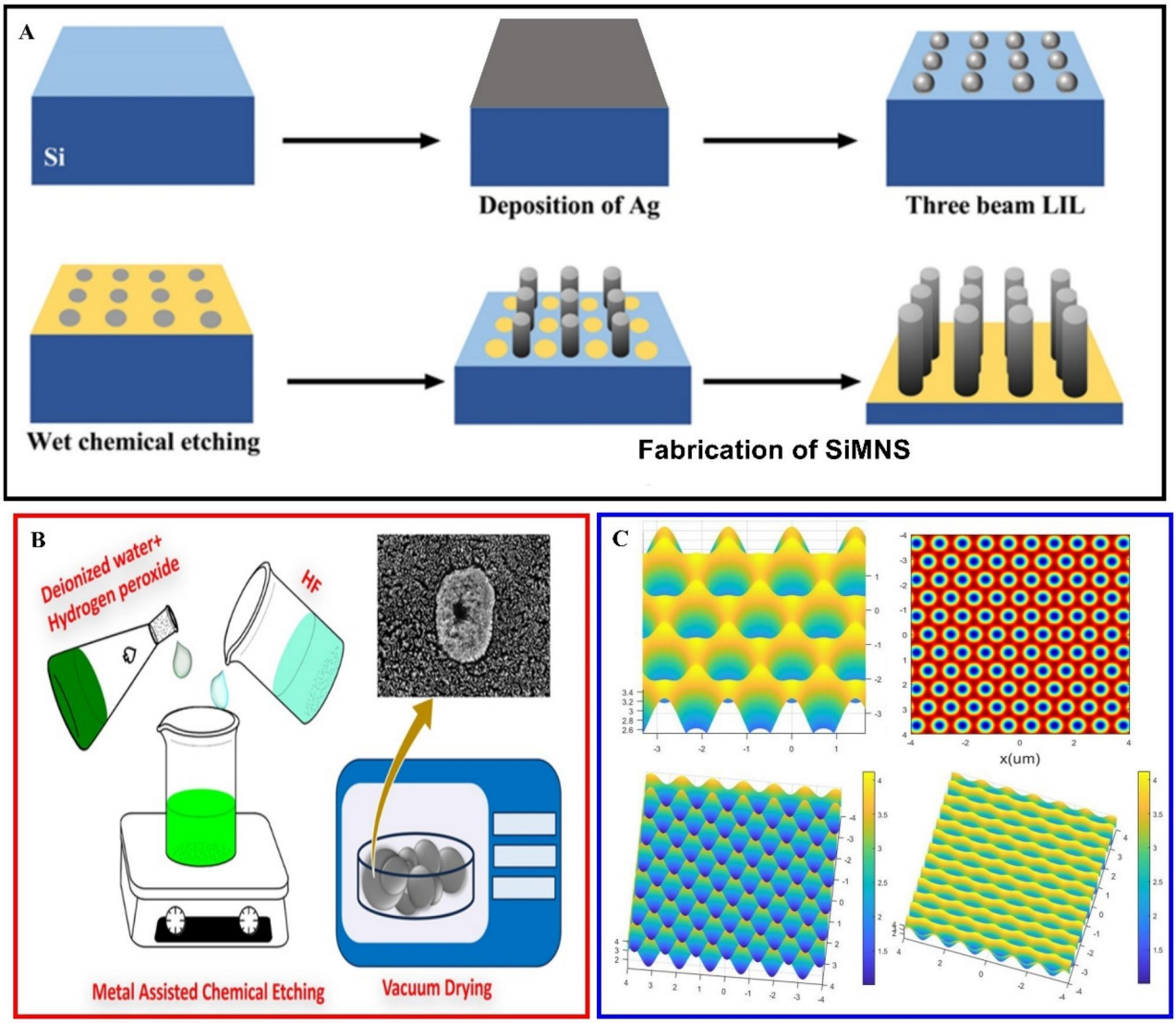

Figure 2. Schematic illustration of the fabrication process for SiMNs. (A) The process involved depositing metal nanoparticles on the Si surface, followed by wet chemical etching to create SiMNs. (B) Diagram of the MACE setup showing the chemicals used, including deionized water, hydrogen peroxide, and hydrofluoric acid (HF). (C) Simulated three-dimensional and two-dimensional patterns of the SiMNs.

a uniform array of structures on the Si substrate. The etching solution generates a localized redox reaction at the metal-Si interface, promoting anisotropic etching that results in well-defined SiMNs. Subsequently, the samples were rinsed thrice with deionized water and dried to ensure that the SiMNs remained clean and undistorted after etching. Figure 2(C) shows the simulated three-dimensional (3D) and two-dimensional (2D) representations of the resulting arrays. The 3D simulations (top images) highlighted the uniform peaks and valleys formed in the SiMNs, thereby confirming their periodicity. The 2D images demonstrate the spatial arrangement and uniformity across the substrate, showing a hexagonal or periodic grid pattern, which indicates precise control over the etching process. These simulations validate the ability of the experimental setup to produce consistent SiMNs with controlled dimensions, which are crucial for applications in photovoltaics, sensing, and photonic devices, where uniform nanostructure arrays can enhance performance through light trapping, increased surface area, or specific wavelength interactions [44]. All the experiments were conducted in a clean chemical laboratory.

3. Results and discussion

The FDTD simulation optimized the dimensions and periodicity of the Ag micropattern to achieve the desired properties. This FDTD model investigates the interplay between light and microscale structures, including Si(Ag) micropatterns. The texture size-to-wavelength ratio applies to all values, including the constraints on long and short wavelengths [14]. The simulation domain comprising the microarray structure and surroundings was divided into grid cells. The grid cell size depends on the desired spatial resolution and the incident light wavelength. The material properties assigned to the grid cells represent the microparticle structure of Si with Ag coating. Plane waves were used to adjust the incident light. The 2D structure's polarization depends

on its low diffraction efficiency. The unit cell had periodic boundary conditions. The boundary conditions of the simulation domain determine the behavior of the electromagnetic fields at their boundaries. These requirements ensure proper field propagation within the simulation region and prevent reflections from boundaries [45,46]. The refractive indices of Si and Ag determine how light interacts with materials and their optical properties. Refractive indices are often modeled based on theoretical or experimental values and are determined as a function of wavelength.

FDTD advances the electromagnetic field over time. The simulation involves multiple phases to allow the fields to propagate and interact with the structure. The electric and magnetic fields following Ag coating and structure are shown in Figure 3. The fields were positioned at the edges of the domain to determine the reflectance and transmittance. The simulation patterns show the 3D electromagnetic field distribution, the geometry of the hole constructs, and changes in material layers. The region where the incident light (or other electromagnetic radiation) interacts with the Ag coating is represented by the uppermost layer in the image, which appears in a range of colors, from red to yellow. The color intensity is proportional to the amount of light reflected by the Ag coating. The vast blue area beneath the cover indicates the Si substrate. The absence of high-intensity colors (such as red or yellow) at the top of the material interface indicates low reflectance, or conversely, high absorption or transmission. The dark blue color, which dominates most of the substance, implies that the simulated quantity is present at low levels within the material. This demonstrates the effects of the laser on the reflectance, absorption transmittance, and structural integrity of the Ag coating. Figure 3(A–E) depicts a color map of the expected total reflectance and transmittance for the micro-and nano-structures as a function of the wavelength (300–1100 nm) and diameter (4–100 nm) at normal incidence. The transmittance was tuned to a period of 100 nm and 428 THz was chosen as the frequency. The minimum reflectance at normal incidence

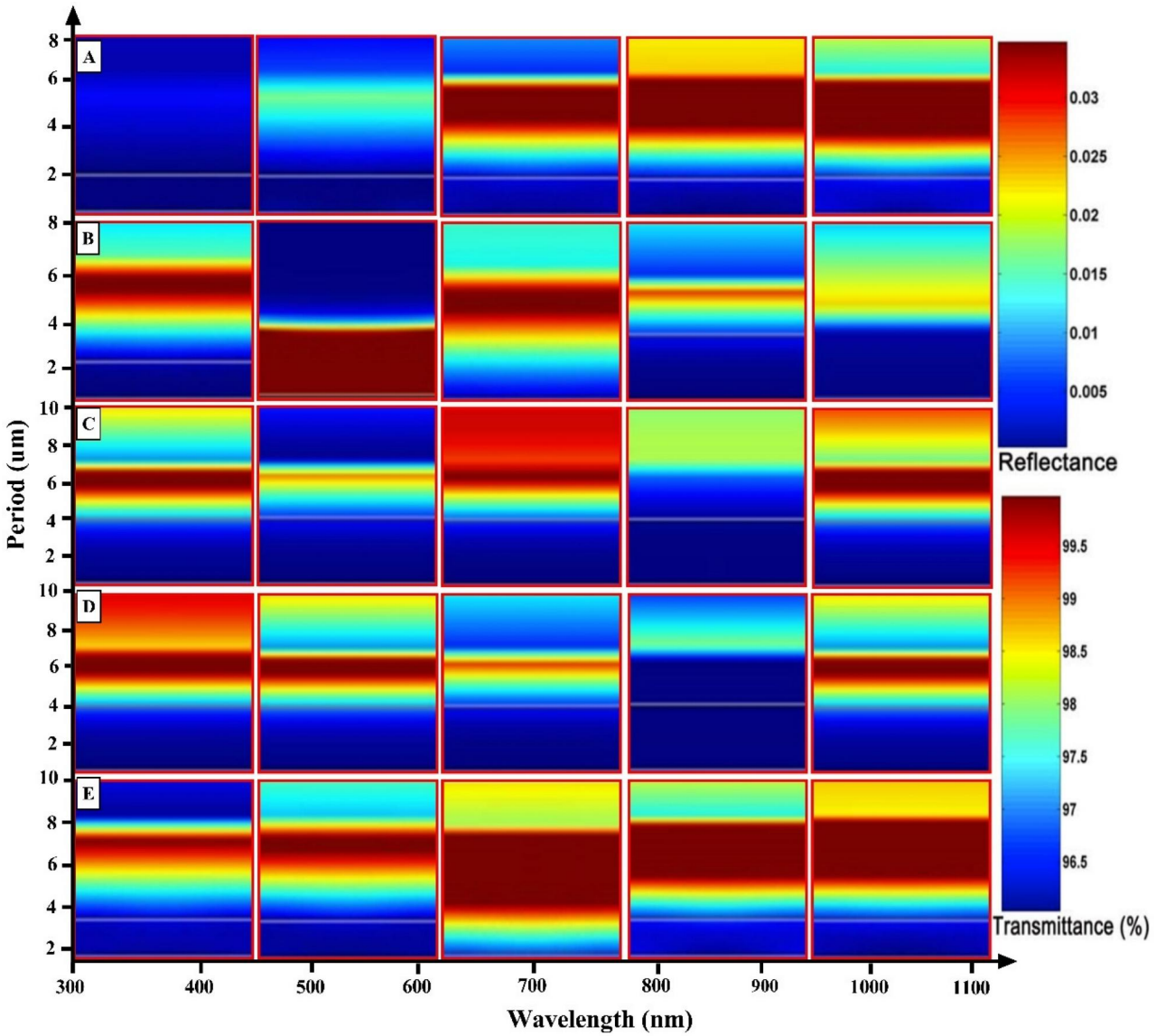

Figure 3. Simulation results of micropattern array FDTD light propagation (A–E) spectrum analysis of reflectance and transmittance as a function of wavelength (300–1100 nm).

on the substrate with 4 nm diameter nanostructures was observed to be less than 0.5. In Figure 3(A–E), the period of the micropattern refers to the spatial interval between adjacent features in the pattern. This period is essential for understanding the size and arrangement of microstructures across the substrate [47]. The period values are represented on the x-axis, corresponding to the wavelength range from 300 to 1100 nm, with the micropatterns being influenced by these wavelengths. Each subplot (A, B, C, D, and E) shows how the periodicity of the patterns changed across different wavelengths. It is essential to highlight that the period can affect the optical properties and performance of a material, such as light diffraction or absorption [48]. The period of the micropatterns in Figure 3(A–E) was determined by the spacing between adjacent microstructures within each pattern [49,50].

In TBLIL, the period can be influenced by the wavelength of the laser light used in the patterning process, where the spacing of the micropatterns is controlled by the interference of the light beams [51].

$$p = \frac{\lambda}{\sin\theta}$$

A scanning electron microscope (SEM; FEI Quanta 250 FEG) was used to characterize the surface morphologies of the laser-treated samples. The SEM images in Figure 4 illustrate the effect of nanosecond LIL on Si-Ag surfaces, with varying Ag coating thicknesses (20 nm, 30 nm, 35 nm, 40 nm, 45 nm, and 50 nm) influencing the resulting nanopattern morphology. These patterns are the result of laser interference, where the intensity distribution is influenced by the laser parameters, including the number of laser beams, incident angles, azimuthal angles, and polarization directions [37,52]. As the Ag thickness increased, the periodicity and clarity of the micropatterns also changed, with a noticeable shift in the size and definition of the hexagonal structures [53,54]. Figure 4(A) shows a high-density array of Ag nanoparticles formed on Si, with the pattern intricately defined by precise adjustments in the laser parameters. This indicated that the laser intensity distribution was sufficiently uniform to create consistently sized particles across the sample area. Figures 4(A–C) show a well-defined hexagonal pattern with 20 nm Ag thickness, with a period of approximately 5.5 μm is visible. This pattern is consistent with the results of the three-beam laser interference simulation, which also predicts a hexagonal distribution. Figure 4(D) shows that the Ag thickness

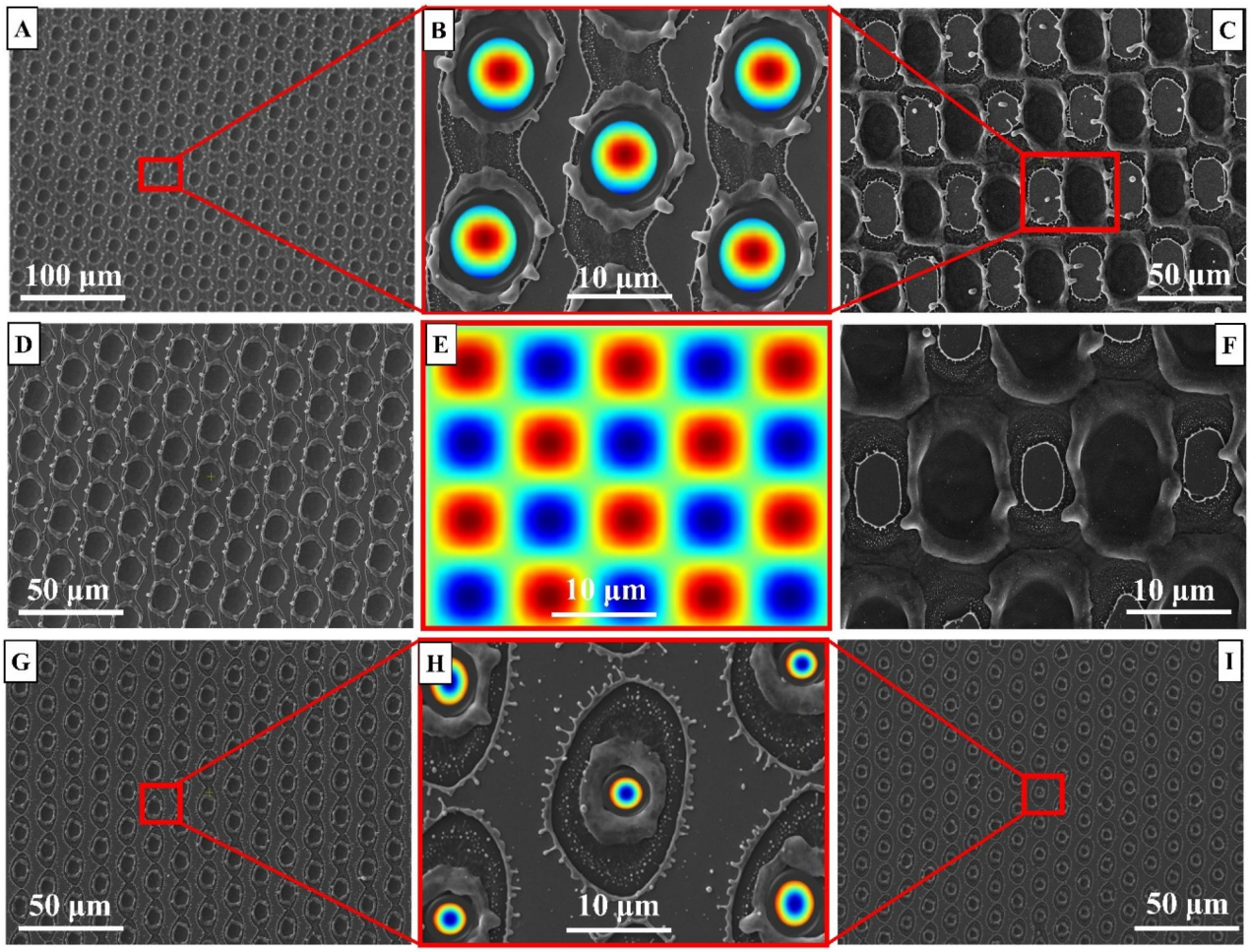

Figure 4. SEM images of Si-Ag structures after TBLIL. (A) Large-area view of the patterned Si surface with a magnified section showing highly periodic circular microstructures on a scale of 100 µm. (B, C) Closer view of the microstructure pattern with the Central section displaying the simulated interference pattern. The periodic square array pattern closely aligns with the experimental SEM results, confirming that the TBLIL setup successfully created uniform arrays with controlled spacing and size. (D) Micropatterns at 50 μm thickness. (E) Periodic pattern formation at a scale of 10 μm. (F) Close-up view of the patterns at the 10 μm scale. (G) Vertical region of Si substrate showing elliptical microstructures. (H) The zoomed-in SEM images emphasize consistency in the pattern shape and arrangement achieved through precise TBLIL exposure. (I) close-up of the patterns at the 50 μm scale.

increases to (30) nm, and the micropatterns become more prominent with increasing size and improved definition of the hexagonal features; a squarely distributed oval shape pattern with a period of approximately 8–10 μm is formed, highlighting how the number of laser beams and their configuration significantly impacts the resulting surface patterns. The variations in Ag thickness and laser parameters lead to distinct periodic patterns, revealing the intricate relationship between material properties and laser interference techniques in microfabrication. 4(E) shows the laser intensity distribution across the surface simulated using MATLAB. The intensity profile is color-coded, with red and blue regions indicating high-and low-intensity zones, respectively. Figure 4(G–I) shows the corresponding SEM image at 40–50 nm Ag coating beside it shows SiMN structures, suggesting that high-intensity laser pulses induced dewetting in these zones, leading to the selective formation of oval shape structures [42]. This shows a different structural arrangement of Ag nanoparticles, which is attributed to changes in incidence and polarization angles. These laser-induced structures display an ordered periodic pattern, in which high-energy interference is selectively eliminated at precise locations, leaving behind defined nanopatterns. This selective fabrication allows fine control over the depth, size, and spacing of nanostructures. This study demonstrated the potential of nanosecond LIL for dynamically controlling Si surface patterning, enabling customizable nanopatterns for applications requiring specific optical and electrical properties.

Figure 5 indicates that by varying the laser voltage, energy input, Ag coating, and beam configuration, it is possible to tailor the morphology of arrays with diameters ranging from 4 to 300 nm. The SEM images illustrate the impact of these parameters on structure size and pattern formation. The TBLIL laser beam diameter ranges from 1 to 2 mm. Figure 5(A) shows an array of oval-shaped micropatterns with diameters ranging between 200 and 300 nm. This patterning is the result of specific laser conditions, such as the controlled beam voltage and energy input, which are optimized to produce larger features [52]. The spacing between these patterns was noticeable, suggesting a coarser arrangement of the micropatterns formed under the experimental conditions, including the Ag coating and beam configuration [55]. Figure 5(B) shows a closer view of the same patterning, in which the individual structures appear smaller and more refined. Here, the diameter of the oval-shaped structures is approximately 100–200 nm, which shows a reduced pattern size compared to that in Figure 5(A). The reduction in structural size is due to a variation in the laser fluence, energy input, and potentially thinner Ag coating [56]. This demonstrates that, by fine-tuning the laser parameters, including the beam configuration, it is possible to achieve smaller and more tightly defined patterns. Figure 5(C) shows a broader

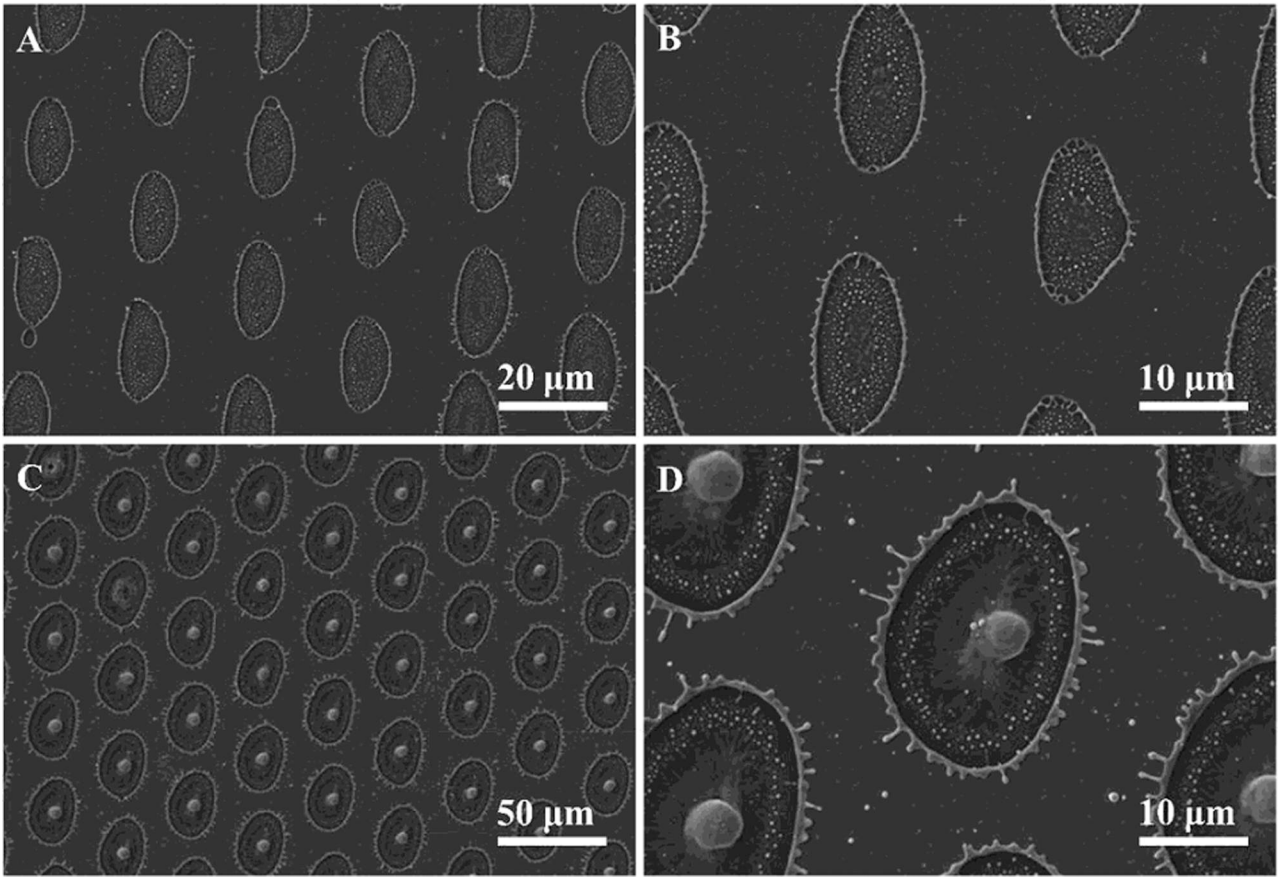

Figure 5. SEM images of Si-Ag structures with different coatings and laser fluences after TBLIL. (A) Oval shape micro patterns with low laser fluence. (B) Close view of micro patterns at low fluence. (C) Larger array of structures at high laser fluence. (D) Close view of micro patterns at high laser fluence.

field of view, showing a larger array of structures. The individual patterns in this image are in the 200–400 nm range, indicating a larger structure size, likely influenced by the laser voltage and energy input, which favored broader, more widely spaced patterns. This variation suggests that increasing certain parameters, such as laser energy, can result in larger micropatterns [57]. Figure 5(D) shows a detailed zoomed-in at the micropattern scale of 10 µm at high laser fluence. The structures were approximately 100–300 nm in diameter, and the details of the patterns were much clearer. The image reveals finer features resulting from optimizing the experimental conditions for smaller pattern sizes. These smaller structures correspond to a more precise laser setup or more uniform Ag coating, allowing for a higher resolution and smaller diameter patterns. By adjusting the laser voltage, energy input, Ag coating, and beam configuration, it was possible to fabricate patterns with diameters ranging from 100 nm to several micrometers, demonstrating the flexibility and precision of the TBLIL process in producing custom SiMNs.

The process of creating SiMN arrays using MACE and TBLIL is illustrated in Figure 6. The initial phase involves the precise placement of silver nanoparticle (AgNP) arrays on a Si substrate. These AgNPs, patterned using TBLIL, served as templates for the subsequent etching process in HF and H_2O_2 solutions. By applying alternating laser fluences to the AgNPs, distinct patterns were obtained, which guided the etching process and shaped the SiMNs. This approach allows detailed control of geometry and produces highly ordered arrays with remarkable crystallinity. One of the critical findings illustrated in Figure 6 is the capacity to fine-tune the dimensions of the SiMNs through careful parameter adjustments in the MACE process. The periodicity of the SiMNs was maintained at approximately 7–10 µm, whereas their length varied from 600 to 1310 nm, with an average of approximately 1092 nm. The length variations were primarily influenced by the duration of the etching process, demonstrating that the SiMN depth could be modulated by controlling the etching time and reagent concentration.

Figure 6(B,D,F,H) shows Atomic Force Microscopy (AFM) images to measure the depth of the SiMNs, providing a topographical view of the nanostructures. AFM analysis showed that the depths of the SiMNs varied with the etching time and thickness of the Ag catalyst. The samples in the images displayed depths ranging from 1130 to 1600 nm, with an average depth of approximately 1295 nm. The correlation between depth and etching time suggests a consistent and controlled etching process, where longer etching produces deeper structures. This level of control is advantageous for applications that require specific depth profiles, making MACE a versatile technique for creating nanostructures with customizable dimensions. Further insights from Figure 6 reveal a direct relationship between the thickness of the Ag film and the depth of the resulting SiMNs. As shown in the data, a thicker Ag catalyst resulted in deeper etching, which can be used to tailor the SiMN morphology by adjusting the thickness of the initial Ag layer. This capability provides a straightforward means of controlling the aspect ratio, which is essential for optimizing micro/nanostructures for optical, electronic, and sensing applications. The linear relationship between the Ag film thickness and SiMNs depth underscores the importance of catalyst layer properties in the etching process. The concentration of H_2O_2 in the HF/H_2O_2 etching solution played a crucial role in controlling the etching rate and stability of the Si substrates. In this study, the H_2O_2 concentration was varied from 1.5 mL to 2 mL, and it was found that higher concentrations of H_2O_2 resulted in increased etching rates and more stable etching characteristics. Similar findings have been reported in previous studies [58–62], which demonstrated the impact of H_2O_2 concentration on etching outcomes. Finally, the role of the H_2O_2 concentration in the HF/H_2O_2 etching solution is evident as it significantly influences the etching rate and stability of the nanostructures [58,63,64]. A careful balance of the reagent concentrations ensured uniform etching across the Ag/Si interface, yielding consistent nanostructures with minimal defects. This level of control over the etching environment and catalyst design further highlights the effectiveness of combining TBLIL and MACE for fabricating Si nanostructures with desired properties. Figure 6 demonstrates the potential of the TBLIL and MACE techniques for producing SiMN arrays with precise dimensional and structural characteristics. By manipulating the laser fluence, etching time, Ag layer thickness, and chemical concentration, this method enabled the fabrication of customizable nanostructures. The findings underscore the versatility and precision of this approach, making it suitable for applications in light harvesting, sensor development, and other nanotechnology fields that demand high control over nanostructure morphology.

Figure 7 shows cross-sectional SEM images of SiMNs structures with feature sizes of 50 μm and periods of 13 μm, 15 μm, 16, and 17 μm, respectively. It can be seen that the SiMNs structure has smooth sidewalls ridges, and sharp tips. Figure 7(A) shows well-defined V-shaped grooves with sharp edges, and uniform periodicity, indicating the high precision of the TBLIL process. The inset in the image provides a magnified view of a single groove, highlighting the clean, smooth sidewalls and the depth of approximately

Table 1. Three-beam LIL and MACE system parameters.

Sample Si (Ag)	Laser fluence (mJ cm^{-2})	Pulse energy (mJ)	Exposure duration (ns)	Polarization mode	Depth (um)
20	560	40	7–9	TE-TE-TE	4.1
30	580	50	7–9	TE-TE-TM	4.33
35	600	40	7–9	TE-TE-TM	4.7
40	650	40	7–9	TE-TE-TE	5.6
45	700	50	7–9	TE-TE-TM	6.9
50	750	50	7–9	TE-TE-TM	7.52

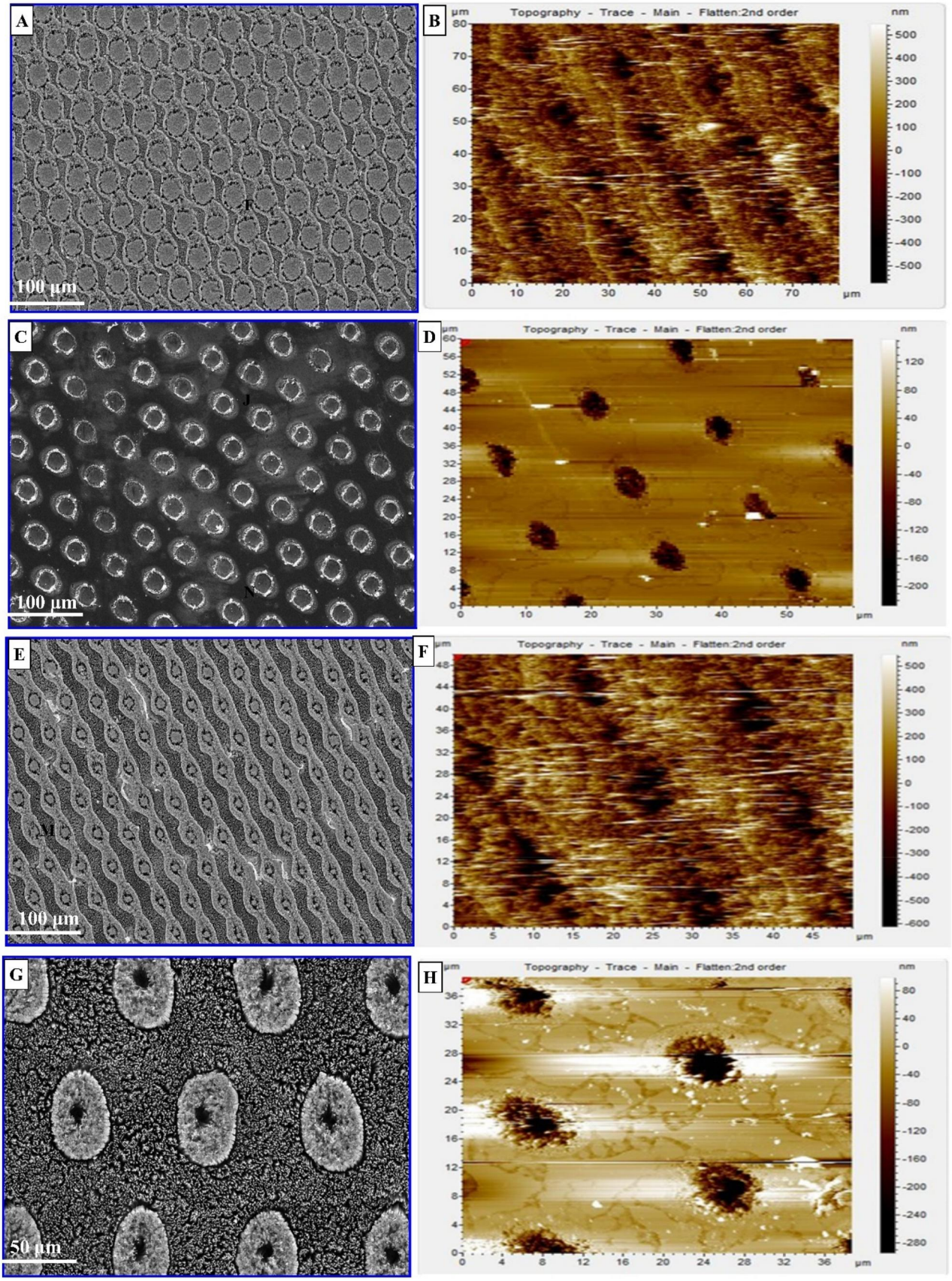

Figure 6. SEM, and AFM, images of the SiMN arrays. (A, C, E, G) SEM images of periodic SiMN arrays with different morphologies were obtained by varying laser fluence and etching conditions. (B, D, F, H) AFM images illustrating the topographical depth of the SiMNs, with depths ranging from 1130 to 1600 nm, correlated with the etching duration.

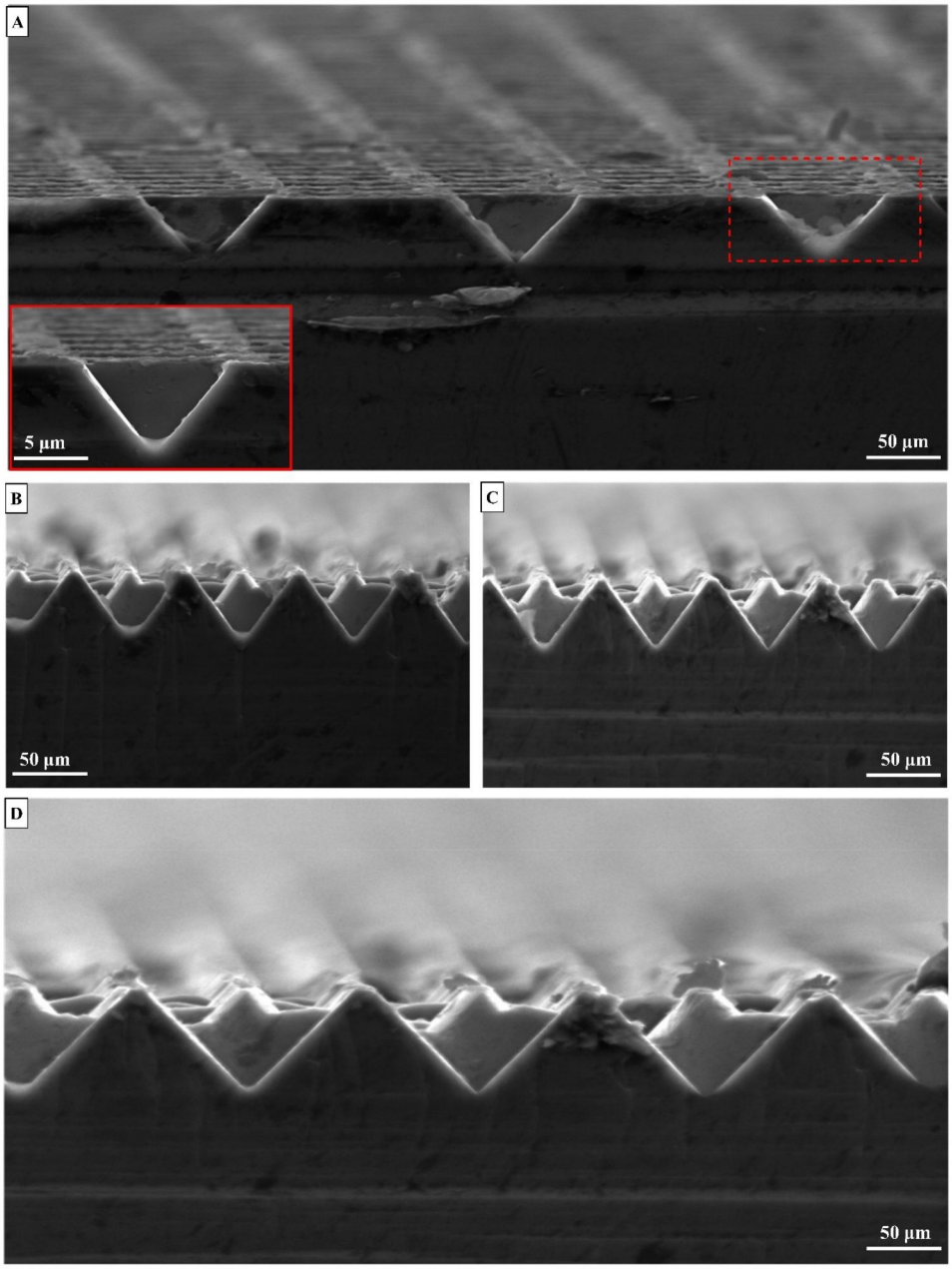

Figure 7. Cross-sectional SEM images of SiMNs fabricated by TBLIL and MACE. (A) V-shaped grooves at 50 um. (B–D) SiMNs with increased etching depth, showing uniform periodicity and sharp profiles.

(3.31–4.7) µm, which reflects the controlled etching process. Figures 7(B,C) display the SiMNs with increased etching depth, reaching approximately (4–6) µm, while maintaining structural uniformity and sharpness along the vertical profiles. The consistency in the triangular cross-sectional patterns across these panels demonstrates the reproducibility and stability of the fabrication process under varying etching conditions [65]. Figure 7(D) shows a more pronounced structural modification, where the SiMNs exhibit slightly irregular features with surface roughness, likely due to extended etching durations or variations in etching parameters and depth around (7–8) µm. Overall, these images confirm the effectiveness of the combined lithography and MACE techniques in producing highly ordered, vertically aligned Si micro/nanostructures with tunable depths and sharp geometries, suitable for applications in optoelectronics, sensing, and photonic devices.

3.1. EDS analysis

The Energy-Dispersive X-ray Spectroscopy (EDS) analysis shown in Figure 8 provides an in-depth examination of the elemental composition and spatial distribution within the SiMN arrays created through chemical etching. The EDS spectrum in Figure 8(A) shows distinct peaks corresponding to Si, Ag, and O. The high intensity of the Si peak signifies that Si is the dominant element, forming the primary structure of the substrate and the surrounding matrix of the SiMN arrays. The presence of Ag and O peaks further confirmed the presence of AgNPs and oxide compounds, likely

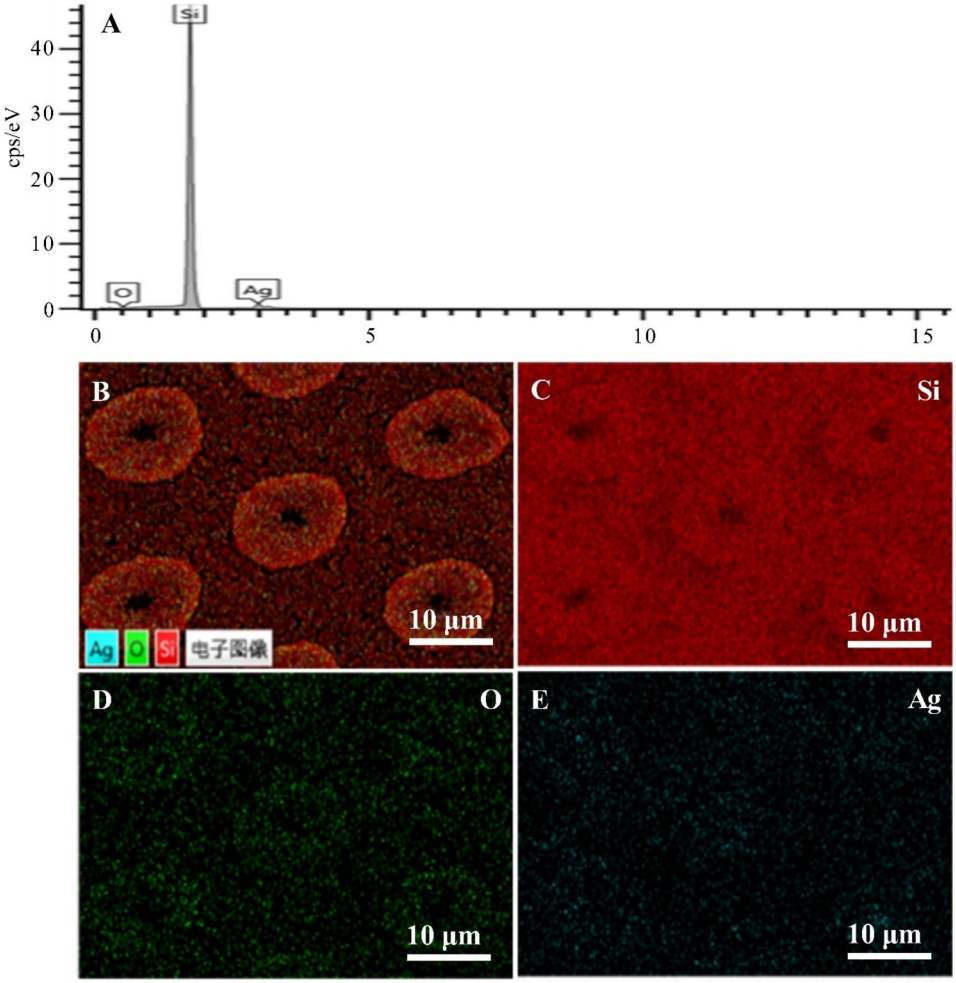

Figure 8. EDS surface analysis of the SiMN arrays. (A) EDS mapping image. (B) EDS analysis of AgNPs on the array surface. (C) Si element. (D) O element. (E) Ag element.

owing to the etching process. This spectrum underscores the successful incorporation of Ag nanoparticles, which act as catalysts during the etching process, and indicates that oxide formation occurs within the structures. Figure 8(B) shows a combined element map of the SiMN array, where each color represents a different element (Si in red, O in green, and Ag in blue). This map illustrates the periodic distribution of elements, mirroring the structural design of the array [66]. This organized distribution suggests that the etching process effectively patterned the SiMN arrays, thereby achieving the desired spatial arrangement of the elements. Figure 8(C,D,E) provide individual maps for each element, highlighting their unique distributions within the array. Figure 8(C) focuses on Si, which is shown in red, indicating its high concentration in the surrounding matrix that forms the structural framework of the arrays. Figure 8(D) highlights the distribution of oxygen in green, predominantly located in the central regions of the SiMNs. Figure 8(E) shows the Ag distribution in blue, illustrating the Ag clusters around the edges of the SiMNs. This spatial arrangement aligns with the role of Ag as a catalyst in the MACE process and reflects its tendency to remain at the edges of structures after etching. This precise elemental distribution is critical for understanding the chemical and physical characteristics of SiMN arrays, as the configuration of elements within the SiMNs can influence their behavior in various applications, such as electronic devices or sensors, where specific elemental layouts may enhance the functionality [67].

4. Antireflection properties

Figure 9 shows a comparative analysis of the theoretical and experimental optical properties of the SiMN arrays, which were designed to reduce surface reflection and enhance light absorption across a broad spectrum (400–1100 nm). This improvement is particularly relevant to solar cell technology, where efficient light absorption can significantly increase energy conversion efficiency. SiMN arrays employ a gradient refractive index (GRIN profile that gradually changes the refractive index at the surface, thereby minimizing light reflection [68,69]. To account for the GRIN profile of the SiMN arrays, the side-view SEM images provide critical insights into the structural features responsible for this optical behavior. The SiMN arrays exhibit a tapered, V-shaped geometry with sharp apexes and gradually sloping sidewalls, as shown in Figures 7(A–D). This tapered morphology facilitates a smooth transition of the refractive index from air to the silicon substrate, effectively creating a GRIN profile. The gradual change in the structural density along

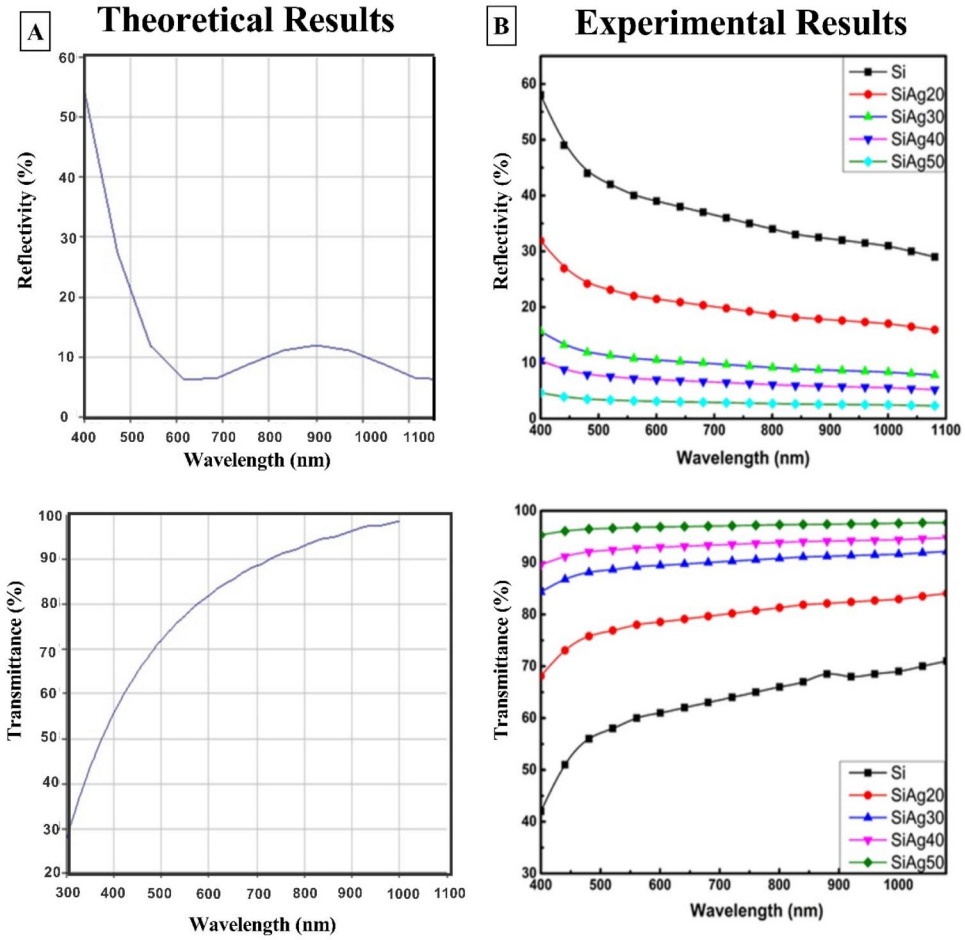

Figure 9. Theoretical and experimental reflectance and transmittance spectra of the fabricated SiMN arrays. (A) Theoretical results for reflectivity and transmittance across various wavelengths. (B) Experimental results for reflectivity and transmittance across various wavelengths.

the vertical direction minimizes the abrupt refractive index contrast at the interface, thereby reducing Fresnel reflections and enhancing light transmission [70]. This is particularly evident in Figures 7(B–D), where the uniform periodicity and increased depth (4–8 μm) of the SiMNs contribute to the gradual refractive index variation. The sharp, well-defined edges and the high aspect ratio of the structures further optimize light trapping and anti-reflective properties. Hence, the side-view SEM images not only confirm the precise fabrication of the SiMN arrays but also substantiate their role in achieving a GRIN profile, which is essential for advanced optoelectronic applications.

Figure 9(A) shows the theoretical results for reflectivity and transmittance across various wavelengths. The theoretical reflectivity curve demonstrated that the reflectance decreased sharply and remained low across the visible to infrared spectra, supporting the theoretical predictions of the GRIN effect. The transmittance curve suggests a corresponding increase in light transmission, reaching approximately 100% in the near-infrared range. These results indicate that SiMN arrays theoretically exhibit low reflectivity and high transmission owing to their GRIN profile and periodic structure, which are designed to facilitate destructive interference and light-trapping [71]. Figure 9(B) presents experimental results, showing the reflectivity and transmittance measurements for different SiMN samples (SiAg20, SiAg30, SiAg40, and SiAg50) with varying Ag coating thicknesses. In the reflectivity graph, bare Si exhibited the highest reflectance, which decreased with increasing Ag thickness on the SiMN arrays. SiAg40 and SiAg50 samples demonstrated the lowest reflectance of approximately 3% across the visible to near-infrared range, supporting the effectiveness of the GRIN profile in reducing surface reflection. The increased Ag coating enhanced the antireflective properties of the SiMN arrays by scattering and confining incoming light within the surface layers, thus minimizing the reflectivity. The transmittance graph further illustrates this behavior, with the SiAg40 and SiAg50 samples displaying the highest transmission rates, reaching approximately 97% across the spectrum. This high transmission is attributed to the thin-film interference effect within the SiMN arrays, where reflections from the top and bottom surfaces create destructive interference, reducing reflectance. In Figure 9, the transmittance discrepancies observed between the theoretical and experimental data, particularly in the 400–800 nm wavelength range, are attributed to several factors. Theoretical models assume ideal conditions such as a perfectly smooth surface and uniform material properties, which do not fully account for real-world conditions [72]. In experimental work, surface roughness and fabrication imperfections in the SiMN arrays and Ag coatings caused light scattering, leading to a

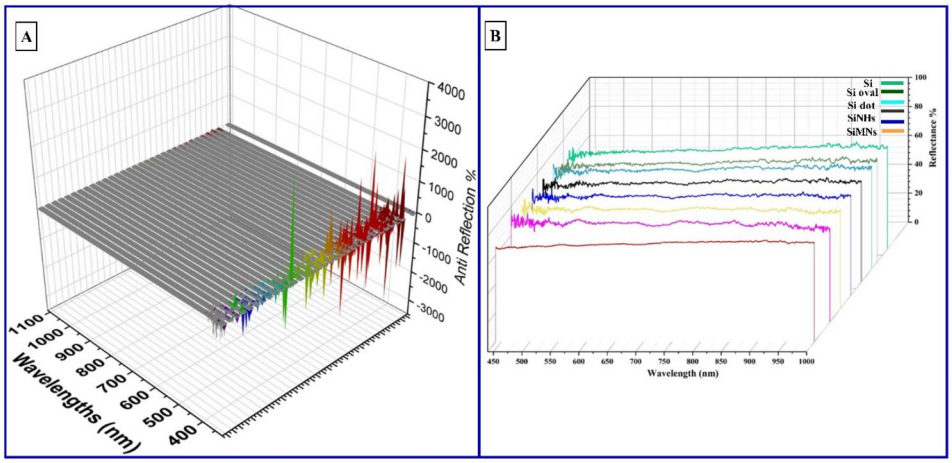

Figure 10. 3D Plots of reflectance spectra of SiMNs with different morphologies, showing reflectance variations at different wavelengths (400–1100 nm). (A) 3D reflectance spectra of the SiMN arrays. (B) comparison of the reflectance spectra for different SiMNs with varying AgNP layer thicknesses.

reduction in the measured transmittance, especially at shorter wavelengths. Additionally, variations in Ag deposition, such as grain boundaries, can alter the optical properties of the material, resulting in differences from the idealized model. The experimental setup, including factors such as light-source divergence, angle of incidence, and detector sensitivity, also contributed to the observed discrepancies [73]. Furthermore, absorption and scattering losses within the material, particularly in the 400–800 nm range, could reduce the transmittance compared with the theoretical predictions.

The experimental transmittance and reflectance trends were closely aligned with the theoretical predictions, confirming the effectiveness of the SiMN arrays for antireflection. Patterned SiMN arrays offer substantial improvements in antireflective performance, making them well-suited for use in photovoltaics and other optoelectronic devices [74,75].

Figure 10(A) shows the 3D reflectance spectra of the SiMN arrays over a broad wavelength range (400–1100 nm) and varying work functions. The graph highlights the significant reduction in reflectance achieved by SiMNs owing to their graded refractive index and enhanced light-trapping properties. The interplay between the SiMN structure and plasmonic effects from AgNPs results in minimized reflectance values across multiple wavelengths. The results reveal how the optical properties of SiMNs can be tuned by adjusting parameters such as the work functions, demonstrating their versatility for different optical applications [76]. Figure 10(B) compares the reflectance spectra for different SiMNs with varying AgNP layer thicknesses of 10, 20, 30, 35, 40, 45, and 50 nm. The 3D plot illustrates the influence of Ag thickness on the reflectance properties of the SiMN arrays. Thicker Ag layers (e.g. 40–50 nm) result in lower reflectance compared to thinner layers (e.g. 10–20 nm). As the thickness of the Ag layer increased, the reflectance decreased owing to the stronger plasmonic effects and enhanced electromagnetic field interactions. This indicates that the thickness of the AgNP layer plays a critical role in optimizing the light transmittance and antireflection performance of the SiMNs.

5. Electrical properties

The electrical properties of the SiMN arrays were assessed by measuring the current-voltage (I-V) characteristics across the source (S) and drain (D) electrodes. Figure 11 illustrates these I-V curves, spanning a bias range from −10 V to 10 V, showing linear (ohmic) and rectifying behaviors. This indicates a versatile electronic response attributed to the transformation of the indirect bandgap of Si into a more conductive direct bandgap within SiMNs [77]. This modification facilitates electron mobility, coupled with a high aspect ratio, and enhances electrical conductivity by offering extended pathways for charge-carrier movement, thereby reducing the resistance and promoting efficient charge transport.

The presence of low reflectance and high absorption in the SiMN arrays stimulated electron excitation, leading to an increase in the current. Notably, the SiAg50 substrate exhibited the highest current, which was attributed to its low reflectivity, as depicted in Figure 11. The depth of the SiMNs within the arrays also influences the charge-carrier mobility, due to its direct impact on charge transport dynamics, surface interactions, and internal electric field distribution that contributes to the higher current response observed in the SiAg50 substrate, which possesses the maximum depth and optimal light-trapping capabilities. Deeper SiMNs provide extended pathways for charge carriers, significantly reducing surface scattering and minimizing the influence of surface defects, dangling bonds, and trap states that typically hinder charge mobility in shallower structures [7,78,79]. This reduction in surface-related recombination enhances carrier lifetime and promotes more efficient charge transport. Additionally, the increased depth facilitates directional charge movement, creating continuous pathways that reduce recombination losses and improve overall charge collection efficiency [80]. The high aspect ratio of deeper SiMNs also leads to enhanced electric field distribution within the structures, which accelerates carrier separation and drift, further boosting mobility. Our cross-sectional SEM images (Figure 7) demonstrate SiMNs with depths

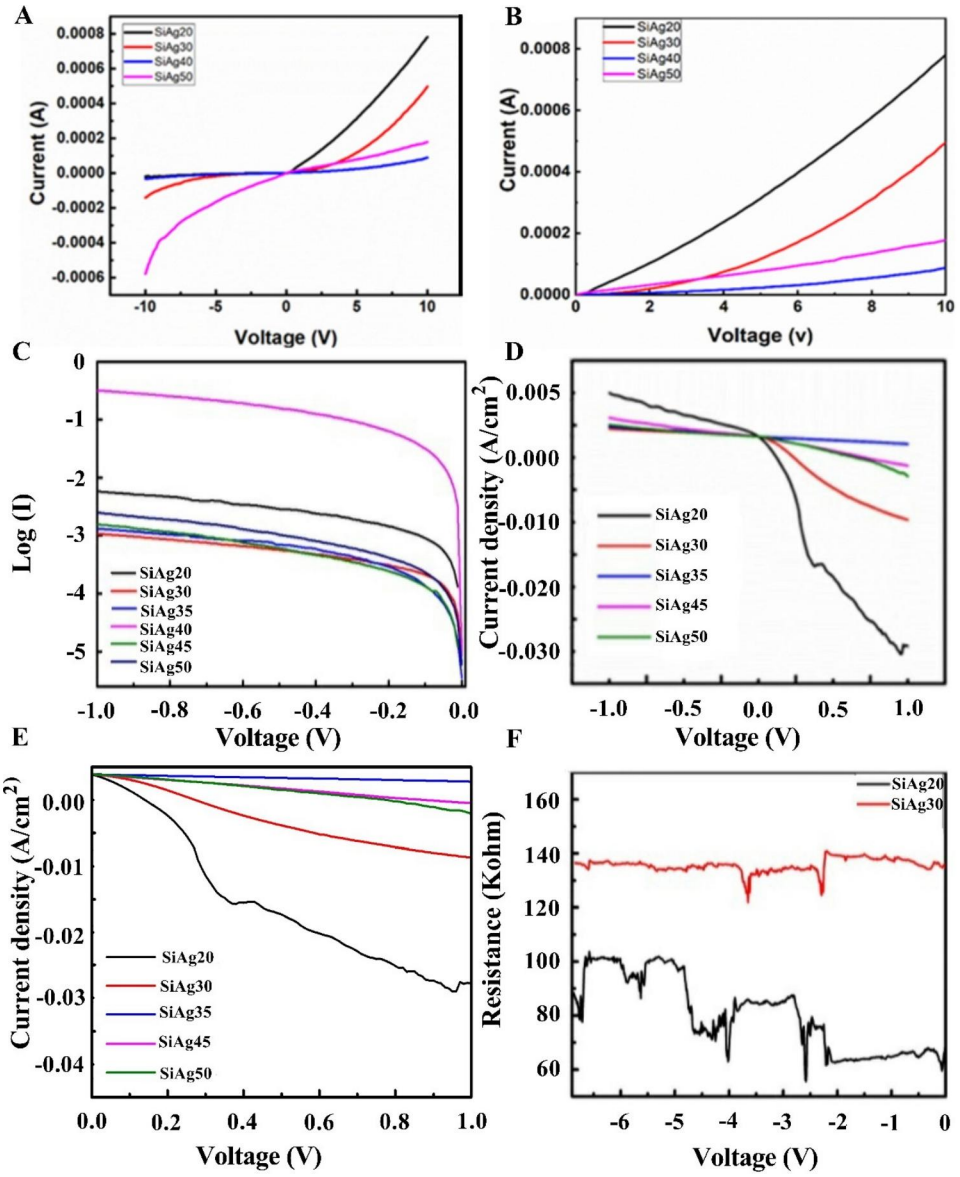

Figure 11. (A, B) I-V characteristic curves of the SiNW diode. (C) V vs. Log I for conduction mechanism of schottky diode. (D, E) The current density-voltage characteristic curve of the Schottky diode for different samples. (F) Voltage resistance curves of electrical properties.

ranging from approximately 4 µm to 8 µm, where deeper structures exhibit uniform alignment and reduced structural defects, correlating with enhanced charge-carrier mobility. Additionally, the structure diameter influences the charge carrier mobility, with smaller diameters facilitating greater mobility, thereby reducing the charge carrier scattering and enhancing the conductivity. The SiAg50 sample emerged as the most conductive, suggesting that its conductance decreased with increasing length, akin to the observed trend where Ag thickness correlates with increased conductance.

The electrical resistance of the SiMN arrays can be determined from the slope of the I-V characteristic curves in Figure 11(A,B) by employing Ohm's law to calculate resistivity [81,82].

$$\rho = \frac{RA}{L} \tag{1}$$

Where R is the resistance, A is the contact area, and L is the contact length.

The rectifying behavior observed is linked to the Schottky diode effect arising from the Ag and SiMN interface, with I-V curves indicating enhanced currents in negative voltage regions, characteristic of metal-semiconductor Schottky contacts [83].

Furthermore, the conduction mechanism in the SiMN samples was analyzed using a log I vs. log V plot (Figure 11(C)) transitions from ohmic behavior at low voltages to space-charge-limited conduction (SCLC) at higher voltages. This shift is attributed to the high surface-to-volume ratio of SiMNs and the influence of surface states and defects or trap states on charge transport, particularly at the Ag/SiMN interface, which is rich in trapping states owing to the presence of oxygen [84].

The following discussion assumes that the effect of the oxygen layer on conductance is minimal because the I-V curves demonstrate good metal-semiconductor properties [8,85]. According to these results, smaller, shorter nanowires have higher conductance than larger, longer nanowires, which aligns with what has been observed in recent studies.

Quantitative analysis can be performed using the well-known metal-semiconductor contact thermionic emission model. This model can simulate the I-V characteristics of a Schottky contact with a p-type semiconductor in series. By modifying the experimental I-V characteristics using the Richardson-Schottky diode equation and accounting for the series resistance, diode characteristics such as the ideality factor (n), series resistance (R_s), and diode saturation current (I_s) can be obtained [86,87].

$$I = I_s\left[\exp\left(\frac{q(V - R_sI)}{nk_BT}\right) - 1\right] \tag{2}$$

where q is the electron charge, V is the applied voltage, k_B is Boltzmann's constant, T is the absolute temperature and I_S is the reverse-saturation current.

$$I_s = AA * T^2 \exp\left(-\frac{\phi_B}{kT}\right) \tag{3}$$

A denotes the contact area, A* denotes Richardson's constant, and B denotes the Schottky barrier height (SBH) between the metal tip and the Si nanowire. Consequently, the SBH can be derived using the following formula:

$$\phi_B = kT\ln\left(\frac{AA * T^2}{I_s}\right) \tag{4}$$

Figure 11(D,E) highlights the high-speed switching capabilities of the Schottky diode with negligible lagging, thus minimizing power loss. Figure 11(F) depicts a direct relationship between voltage and resistance, indicating an increase in resistance with voltage, validating the findings from four-point resistance measurements, and demonstrating a linear relationship between nanohole resistance and length. These findings align with the existing literature, underscoring the critical role of SiMN arrays in the electrical performance of sophisticated structures and suggesting potential enhancements in SiMN-based solar cells and high-speed electronic devices [87–90]. The morphology of SiMN arrays significantly affects their electrical characteristics, particularly their conductivity, resistivity, and carrier mobility. As the morphology changes with varying Ag thickness and the fabrication process, the number of active sites, the surface area, and the interconnectivity between the nanostructures are altered, all of which influence the overall electrical performance [91,92]. We found that SiMN arrays with finer features, achieved through optimized TBLIL and MACE conditions, exhibited improved electrical conductivity owing to better alignment of the conductive paths and reduced scattering. Additionally, the electrical resistivity was found to decrease as the periodicity and uniformity of the structures improved, particularly in samples with thicker Ag coatings. On the other hand, arrays with less-defined structures showed higher resistivity and lower carrier mobility owing to increased scattering at irregular interfaces.

By combining TBLIL and MACE, it was possible to fine-tune the morphology to optimize both the optical and electrical properties. Our analysis highlights the significant improvements in the electrical properties when using this combined approach, offering superior performance compared with arrays fabricated using either TBLIL or MACE alone. These findings demonstrate the significant impact of morphological control on the electrical properties of SiMN arrays and emphasize the advantages of using TBLIL and MACE in tandem to achieve optimal performance for practical applications.

6. Conclusion

In conclusion, the innovative combination of TBLIL and MACE for fabricating SiMN arrays has demonstrated significant advancements in enhancing both electrical and antireflective properties. This methodology enabled the successful creation of SiMNs, offering meticulous control over the periodicity, shape, depth, and diameter of arrays. The 3D FDTD simulation showed that the reflectance of these designed surfaces can be decreased to an average of less than 3% across a broad spectrum of light, ranging from visible to near-infrared (400–1100 nm), with the experimental results closely matching the predicted forecasts. The resulting SiMNs are characterized by their exceptional conductivity and superior optical attributes, positioning them as prime candidates for integration into electronic devices. This dual enhancement in the electrical conductivity and antireflection efficiency within a singular hierarchical architecture provides a versatile foundation for advanced nanomaterial engineering. Moreover, the LIL and MACE production processes are both scalable and economically viable, promising pathways for widespread industrial application and commercialization. The convergence of innovative fabrication techniques, improved material properties, and cost-effective scalability have led to a new era in the development of nanotechnology-based solutions for electronic and photonic devices.

Acknowledgment

This work was supported by the Shenzhen Science and Technology Program (Shenzhen Key Laboratory of Ultrafast Laser Micro/Nano Manufacturing ZDSYS20220606100405013), National Natural Science Foundation of China (U22A2088).

Author contributions

Conceptualization: SS and ZW. Methodology: US and AZ. Writing—original draft preparation: SS. Writing—review and editing: AZ, CL, US, and ST. Supervision: ZW and CL. Project administration: ZW. Funding acquisition: ZW. All authors have read and agreed to the published version of the manuscript.

Disclosure statement

No potential conflict of interest was reported by the author(s).

Data availability statement

Data underlying the results presented in this paper are not publicly available at this time but may be obtained from the authors upon reasonable request.

References

[1] O.R. Onisuru and O. Onisuru, Smart nanomaterials: fundamentals, synthesis, and characterization. In: Smart Nanomaterials for Environmental Applications, Elsevier, Amsterdam; pp. 117–140, 2025.

[2] Z. Mamiyev, and N.O. Balayeva, PbS nanostructures: a review of recent advances, Mater. Today Sustain., vol. 21, pp. 100305, 2023. DOI: 10.1016/j.mtsust.2022.100305.

[3] N.S. Seroka, R. Taziwa, and L. Khotseng, Solar energy materials-evolution and niche applications: a literature review, Materials, vol. 15, no. 15, pp. 5338, 2022. DOI: 10.3390/ma15155338.

[4] H. Wang, D. Deng, Z. Zhai, and Y. Yao, Laser-processed functional surface structures for multi-functional applications-a review, J. Manuf. Processes., vol. 116, pp. 247–283, 2024. DOI: 10.1016/j.jmapro.2024.02.062.

[5] S. Singh, S. Das, and S.K. Ray, Progress in group-IV semiconductor nanowires based photonic devices, Appl. Phys. A, vol. 129, no. 3, pp. 216, 2023. DOI: 10.1007/s00339-023-06483-7.

[6] T.R. Arunprasand, and P. Nallasamy, Advancements in optimizing mechanical performance of 3d printed polymer matrix composites via microstructural refinement and processing enhancements: a comprehensive review, Mech. Adv. Mater. Struct., vol. 31, pp. 1–19, 2024. DOI: 10.1080/15376494.2024.2426776.

[7] S. Raman, R.S. A, and S. M, Advances in silicon nanowire applications in energy generation, storage, sensing, and electronics: a review, Nanotechnology, vol. 34, no. 18, pp. 182001, 2023. DOI: 10.1088/1361-6528/acb320.

[8] S. Rai, R. Bhujel, M.K. Mondal, B.P. Swain, and J. Biswas, Study of the morphological, optical, structural and electrical properties of silicon nanowires at varying concentrations of the catalyst precursor, Mater. Adv., vol. 3, no. 6, pp. 2779–2785, 2022. DOI: 10.1039/D1MA01145F.

[9] Q. Wang, J.J. Li, Y.J. Ma, X.D. Bai, Z.L. Wang, P. Xu, C.Y. Shi, B.G. Quan, S.L. Yue, and C.Z. Gu, Field emission properties of carbon coated Si nanocone arrays on porous silicon, Nanotechnology, vol. 16, no. 12, pp. 2919–2922, 2005. DOI: 10.1088/0957-4484/16/12/032.

[10] Z. Shi, K. Jefimovs, M. Stampanoni, and L. Romano, High aspect ratio arrays of Si nano-pillars using displacement Talbot lithography and gas-MacEtch, Mater. Sci. Semicond. Process., vol. 157, pp. 107311, 2023. DOI: 10.1016/j.mssp.2023.107311.

[11] A.A. Ermina, N.S. Solodovchenko, K.V. Prigoda, V.S. Levitskii, V.O. Bolshakov, M. Yu. Maximov, Y.M. Koshtyal, S.I. Pavlov, V.A. Tolmachev, and Y.A. Zharova, Silver particles embedded in silicon: the fabrication process and their application in surface enhanced Raman scattering (SERS), Appl. Surf. Sci., vol. 608, pp. 155146, 2023. DOI: 10.1016/j.apsusc.2022.155146.

[12] D. Trapani, R. Macaluso, I. Crupi, and M. Mosca, Color conversion light-emitting diodes based on carbon dots: a review, Materials, vol. 15, no. 15, pp. 5450, 2022. DOI: 10.3390/ma15155450.

[13] A. Lavigne, T. Géhin, B. Gilquin, V. Jousseaume, M. Veillerot, C. Botella, C. Chevalier, C. Jamois, Y. Chevolot, M. Phaner-Goutorbe, and C. Yeromonahos, Effect of silane monolayers and nanoporous silicon surfaces on the matrix-assisted laser desorption ionization mass spectrometry detection of sepsis metabolites biomarkers mixed in solution, ACS Omega, vol. 8, no. 31, pp. 28898–28909, 2023. DOI: 10.1021/acsomega.3c04266.

[14] T. Bartschmid, A. Farhadi, M.E. Musso, E.S.A. Goerlitzer, N. Vogel, and G.R. Bourret, Self-assembled au nanoparticle monolayers on silicon in two-and three-dimensions for surface-enhanced Raman scattering sensing, ACS Appl. Nano Mater., vol. 5, no. 8, pp. 11839–11851, 2022. DOI: 10.1021/acsanm.2c01904.

[15] A. Alsolami, H. Hussain, R. Noor, N. AlAdi, N. Almalki, A. Kurdi, T. Tabbakh, A. Zaman, S. Alfihed, and J. Wang, Recent advances in black silicon surface modification for enhanced light trapping in photodetectors, Appl. Sci., vol. 14, no. 21, pp. 9841, 2024. DOI: 10.3390/app14219841.

[16] B.A. Taha, A.J. Addie, A.C. Kadhim, A.S. Azzahrani, N.M. Ahmed, A.J. Haider, V. Chaudhary, and N. Arsad, Plasmonic-enabled nanostructures for designing the next generation of silicon photodetectors: trends, engineering and opportunities, Surf. Interfaces, vol. 48, pp. 104334, 2024. DOI: 10.1016/j.surfin.2024.104334.

[17] W. Wang, and L. Qi, Light management with patterned micro- and nanostructure arrays for photocatalysis, photovoltaics, and optoelectronic and optical devices, Adv. Funct. Mater., vol. 29, no. 25, pp. 1807275, 2019. DOI: 10.1002/adfm.201807275.

[18] T.M.S. Ashrafi, and G. Mohanty, Surface plasmon resonance sensors: a critical review of recent advances, market analysis, and future directions, Plasmonics, vol. 20, pp. 1–21, 2025. DOI: 10.1007/s11468-024-02740-4.

[19] Y. Liang, W. Ran, D. Kuang, and Z. Wang, Design strategies and insights of flexible infrared optoelectronic sensors, J. Semicond., vol. 46, no. 1, pp. 011602, 2025. DOI: 10.1088/1674-4926/24080044.

[20] C. Chen, L. Shen, B. Wang, X. Lu, S. Raza, J. Xu, B. Li, H. Lin, and B. Chen, Environmental applications of metal–organic framework-based three-dimensional macrostructures: a review, Chem. Soc. Rev., no. 4, pp. 1637–2128, 2025. DOI: 10.1039/d4cs00435c.

[21] A.K. Padhan, V. Singh, S. Ray, and R.K. Voolapalli, High-performance multi-functional solar panel coatings: recent advances, challenges, strategies and industrial aspects, RSC Appl. Polym., vol. 3, 2025. DOI: 10.1039/D4LP00295D.

[22] G. Oh, Y. Kim, S.J. Lee, and E.K. Kim, Broadband antireflective coatings for high efficiency InGaP/GaAs/InGaAsP/InGaAs multi-junction solar cells, Sol. Energy Mater. Sol. Cells, vol. 207, pp. 110359, 2020. DOI: 10.1016/j.solmat.2019.110359.

[23] M. Malinauskas, A. Žukauskas, S. Hasegawa, Y. Hayasaki, V. Mizeikis, R. Buividas, and S. Juodkazis, Ultrafast laser processing of materials: from science to industry, Light. Sci. Appl., vol. 5, no. 8, pp. e16133, 2016. DOI: 10.1038/lsa.2016.133.

[24] X. Liu, B. Radfar, K. Chen, T.P. Pasanen, V. Vähänissi, and H. Savin, Tailoring femtosecond-laser processed black silicon for reduced carrier recombination combined with> 95% above-bandgap absorption, Adv. Photon. Res., vol. 3, no. 4, pp. 2100234, 2022. DOI: 10.1002/adpr.202100234.

[25] M.K. Crawford, L. Fair, K. Rovito, T. Polidori, and R. Grayburn, Thickness measurements of clear coatings on silver objects using fiber optic reflectance spectroscopy, J. Am. Inst. Conserv., vol. 61, no. 2, pp. 71–84, 2022. DOI: 10.1080/01971360.2020.1812317.

[26] R. Karmakar, M. Dixit, A.K. Rengan, and F. Pati, Nanostructures Using 3D Printing. Advances in Nanostructures, Elsevier, Amsterdam, Netherlands, pp. 195–229, 2025.

[27] A. Palevicius, G. Janusas, U. Cigane and J. Ciganas, Analysis of the Microstructure Formation Process. Nano/Micro Functional Elements Formation for Bioengineering Applications, Springer, Switzerland; p. 7–34, 2025.

[28] F. Zhang, and H.Y. Low, Ordered three-dimensional hierarchical nanostructures by nanoimprint lithography, Nanotechnology, vol. 17, no. 8, pp. 1884–1890, 2006. DOI: 10.1088/0957-4484/17/8/013.

[29] S. Sun, P. Lu, J. Xu, L. Xu, K. Chen, Q. Wang, and Y. Zuo, Fabrication of anti-reflecting Si nano-structures with low aspect ratio by nano-sphere lithography technique, Nano-Micro Lett., vol. 5, no. 1, pp. 18–25, 2013. DOI: 10.1007/BF03353727.

[30] B. Ai, H. Möhwald, D. Wang, and G. Zhang, Advanced colloidal lithography beyond surface patterning, Adv. Materials Inter., vol. 4, no. 1, pp. 1600271, 2017. DOI: 10.1002/admi.201600271.

[31] S.C. Calvimontes, R. Rodríguez-Ramos, P. Rodríguez-Bermúdez, J.A.R. Duran, Y. Espinosa-Almeyda, and J.A. Otero, Computational homogenization of linear viscoelastic multiphase composites: Effective relaxation estimation in perovskite-based solar panels, Mech. Adv. Mater. Struct., vol. 32, pp. 1–15, 2025. DOI: 10.1080/15376494.2025.2456105.

[32] K. Akoussan, H. Boudaoud, E.M. Daya, Y. Koutsawa, and E. Carrera, Numerical method for nonlinear complex eigenvalues problems depending on two parameters: application to

three-layered viscoelastic composite structures, Mech. Adv. Mater. Struct., vol. 25, no. 15–16, pp. 1361–1373, 2018. DOI: 10.1080/15376494.2017.1286418.

[33] G. Farid, R. Amade-Rovira, Y. Ma, S. Chaitoglou, R. Ospina, and E. Bertran-Serra, Revolutionizing energy storage: silicon nanowires (SiNWs) crafted through metal-assisted chemical etching, Arabian J. Chem., vol. 17, no. 3, pp. 105631, 2024. DOI: 10.1016/j.arabjc.2024.105631.

[34] F. De Ferrari, S.N. Raja, A. Herland, F. Niklaus, and G. Stemme, Sub-5 nm silicon nanopore sensors: scalable fabrication via self-limiting metal-assisted chemical etching, ACS Appl. Mater. Interfaces, vol. 17, no. 6, pp. 9047–9058, 2025. DOI: 10.1021/acsami.4c19750.

[35] R. Liu, L. Cao, D. Liu, L. Wang, S. Saeed, and Z. Wang, Laser interference lithography—a method for the fabrication of controlled periodic structures, Nanomaterials, vol. 13, no. 12, pp. 1818, 2023. DOI: 10.3390/nano13121818.

[36] Z. Zhang, Z. Wang, D. Wang, and Y. Ding, Periodic antireflection surface structure fabricated on silicon by four-beam laser interference lithography, J. Laser Appl., vol. 26, no. 1, pp. 012010, 2014. DOI: 10.2351/1.4849715.

[37] L. Zhao, Z. Wang, J. Zhang, L. Cao, L. Li, Y. Yue, and D. Li, Antireflection silicon structures with hydrophobic property fabricated by three-beam laser interference, Appl. Surf. Sci., vol. 346, pp. 574–579, 2015. DOI: 10.1016/j.apsusc.2015.04.058.

[38] S. Saeed, A. Zia, R. Liu, D. Liu, L. Cao, and Z. Wang, Optimizing broadband antireflection with Au micropatterns: a combined FDTD simulation and two-beam LIL approach, Appl. Opt., vol. 63, no. 5, pp. 1394–1401, 2024. DOI: 10.1364/AO.514445.

[39] S. Sivasubramaniam, and M.M. Alkaisi, Inverted nanopyramid texturing for silicon solar cells using interference lithography, Microelectron. Eng., vol. 119, pp. 146–150, 2014. DOI: 10.1016/j.mee.2014.04.004.

[40] D. Wang, Z. Wang, Z. Zhang, Y. Yue, D. Li, R. Qiu, and C. Maple, Both antireflection and superhydrophobicity structures achieved by direct laser interference nanomanufacturing, J. Appl. Phys., vol. 115, no. 23, pp. 233101–233106, 2014. DOI: 10.1063/1.4883763.

[41] W. Li, Z. Wang, D. Wang, Z. Zhang, L. Zhao, D. Li, R. Qiu, and C. Maple, Superhydrophobic dual micro-and nanostructures fabricated by direct laser interference lithography, Opt. Eng., vol. 53, no. 3, pp. 034109, 2014. DOI: 10.1117/1.OE.53.3.034109.

[42] D. Zhang, Z. Xin, and Z. Luo, Fatigue behavior of multi-row film cooling holes manufactured by lasers with different pulses under complex-temperature fields, Mech. Adv. Mater. Struct., vol. 31, pp. 1–20, 2024. DOI: 10.1080/15376494.2024.2409413.

[43] I. Kochylas, A. Dimitriou, M.-A. Apostolaki, M.-C. Skoulikidou, V. Likodimos, S. Gardelis, and N. Papanikolaou, Enhanced photoluminescence of R6G dyes from metal decorated silicon nanowires fabricated through metal assisted chemical etching, Materials, vol. 16, no. 4, pp. 1386, 2023. DOI: 10.3390/ma16041386.

[44] T. Barik, K. Pal, P. Sahoo, and K. Patra, Sensor-based strategies for accurate prediction of drilled hole surface integrity of CFRP/Al7075 hybrid stack, Mech. Adv. Mater. Struct., vol. 31, no. 5, pp. 1097–1124, 2024. DOI: 10.1080/15376494.2022.2131945.

[45] M. Hollenbach, N.S. Jagtap, C. Fowley, J. Baratech, V. Guardia-Arce, U. Kentsch, A. Eichler-Volf, N.V. Abrosimov, A. Erbe, C. Shin, H. Kim, M. Helm, W. Lee, G.V. Astakhov, and Y. Berencén, Metal-assisted chemically etched silicon nanopillars hosting telecom photon emitters, J. Appl. Phys., vol. 132, no. 3, pp. 033101-1 - 033101-6, 2022. DOI: 10.1063/5.0094715.

[46] B.M. Rey, R. Elnathan, R. Ditcovski, K. Geisel, M. Zanini, M.-A. Fernandez-Rodriguez, V.V. Naik, A. Frutiger, W. Richtering, T. Ellenbogen, N.H. Voelcker, and L. Isa, Fully tunable silicon nanowire arrays fabricated by soft nanoparticle templating, Nano Lett., vol. 16, no. 1, pp. 157–163, 2016. DOI: 10.1021/acs.nanolett.5b03414.

[47] A. Moradi, R. Ansari, M.K. Hassanzadeh-Aghdam, and J. Jamali, Finite element modeling of the effective creep compliance of carbon nanotube-polymer nanocomposites: a critical microstructure-level investigation, Mech. Adv. Mater. Struct., vol. 31, no. 24, pp. 6109–6125, 2024. DOI: 10.1080/15376494.2023.2225052.

[48] F.I.M. Bincy, S. Oviya, R.S. Kumar, P. Kannappan, S. Arumugam, I. Kim, and S.A.M. Britto Dhas, Investigation of bismuth selenide's structural stability and tunable bandgap under exposure to acoustic shock waves for solar cell and aerospace applications, Mech. Adv. Mater. Struct., vol. 31, pp. 1–15, 2024. DOI: 10.1080/15376494.2024.2413188.

[49] X. Ye, J. Huang, F. Geng, L. Sun, H. Liu, X. Jiang, W. Wu, X. Zu, and W. Zheng, Broadband antireflection subwavelength structures on fused silica using lower temperatures normal atmosphere thermal dewetted Au nanopatterns, IEEE Photonics J., vol. 8, no. 1, pp. 1–10, 2016. DOI: 10.1109/JPHOT.2015.2508723.

[50] S. Zhu, J. Hu, B. Wang, L. Ma, S. Wang, and L. Wu, A fully parameterized methodology for lattice materials with octahedron-based structures, Mech. Adv. Mater. Struct., vol. 28, no. 10, pp. 1035–1048, 2021. DOI: 10.1080/15376494.2019.1629048.

[51] H.E. Etri, M.Z. Polat, and E.B. Özyılmaz, Classification, applications, and impact behavior of composite materials: a review, Mech. Adv. Mater. Struct., vol. 31, no. 30, pp. 12592–12635, 2024. DOI: 10.1080/15376494.2024.2326665.

[52] S. Dalela, P.S. Balaji, and D.P. Jena, A review on application of mechanical metamaterials for vibration control, Mech. Adv. Mater. Struct., vol. 29, no. 22, pp. 3237–3262, 2022. DOI: 10.1080/15376494.2021.1892244.

[53] H.X. Tang, and Z.L. Hu, Application of the Cosserat continua to numerical studies on the properties of the materials, Mech. Adv. Mater. Struct., vol. 24, no. 10, pp. 797–808, 2017. DOI: 10.1080/15376494.2016.1196784.

[54] L. Yao, J. Hu, and X. Kang, Analysis of impact resistance of linear gradient wall thickness circular star thin walled tube, Mech. Adv. Mater. Struct., vol. 32, pp. 1–16, 2025. DOI: 10.1080/15376494.2025.2461285.

[55] J. Li, S. Li, and W. Lin, Actively controllable size-dependent elastic wave band gaps in planar functionally graded micro-lattice, Mech. Adv. Mater. Struct., vol. 31, no. 8, pp. 1678–1698, 2024. DOI: 10.1080/15376494.2022.2141382.

[56] J. Cheng, Z. Yang, S. Jiang, F. Li, and D. Liu, Hybrid laser processes for thick silver coating fabrication on AlN substrate, Ceram. Int., vol. 49, no. 8, pp. 11875–11884, 2023. DOI: 10.1016/j.ceramint.2022.12.035.

[57] J. Ai, M. Lv, M. Jiang, J. Liu, and X. Zeng, Focused laser lithographic system for efficient and cross-scale fabrication of large-area and 3D micro-patterns, Opt. Lasers Eng., vol. 107, pp. 335–341, 2018. DOI: 10.1016/j.optlaseng.2018.04.010.

[58] X. Li, and P. Bohn, Metal-assisted chemical etching in HF/H 2 O 2 produces porous silicon, Appl. Phys. Lett., vol. 77, no. 16, pp. 2572–2574, 2000. DOI: 10.1063/1.1319191.

[59] E. Lee, S. Park, G.-S. Park, M. Mehta, L.Y.S. Lee, C. Kim, and I.-S. Choi, Silicon etching using copper–metal-assisted chemical etching: unveiling the role of Cu2O in microscale structure fabrication, ACS Appl. Mater. Interfaces, vol. 17, no. 1, pp. 2566–2576, 2025. DOI: 10.1021/acsami.4c17500.

[60] P.-Y. Lee, G.-H. Lu, Y.-H. Bai, C.-Y. Chen, L.-Y. Wu, C.-J. Weng, H.J. Huang, and Y.-S. Lin, Hyperspectral analysis of silicon nanowires manufactured through metal-assisted chemical etching, J. Manuf. Sci. Eng., vol. 147, no. 2, pp. 024501, 2025. DOI: 10.1115/1.4066546.

[61] A.A. Helaly, M. Farag, and G. Youssef, Implications of the HF/H2O2 effect on the electrochemical etching formation of macroporous silicon at various etching times, Appl. Phys. A, vol. 131, no. 1, pp. 72, 2025. DOI: 10.1007/s00339-024-08140-z.

[62] Z.-J. Zhao, S.-H. Shin, X. Xu, Y.J. Kim, Z.-P. Yang, S. Hwang, S. Jeon, B. Yu, L. Qian, B.-K. Ju, J.-H. Jeong, and M. Kim, High-uniformity, shape-controlled silicon nanowires for enhanced performance in optoelectronic devices, Small Methods, vol. 9, no. 1, pp. e2402075, 2025. DOI: 10.1002/smtd.202402075.

[63] Z. Huang, N. Geyer, P. Werner, J. de Boor, and U. Gösele, Metal-assisted chemical etching of silicon: a review: in memory

of Prof, Ulrich Gösele. Adv. Mater., vol. 23, no. 2, pp. 285–308, 2011. DOI: 10.1002/adma.201001784.

[64] Z. Yu, R. Wang, Z. Wang, M. Xu, T. Hou, B. Fu, D. Gong, and Y. Shi, Effects of wet chemical etching on surface band bending and electrical properties of Sn-doped β-Ga2O3 (101) substrate, Vacuum, vol. 233, pp. 113959, 2025. DOI: 10.1016/j.vacuum.2024.113959.

[65] T. Tiwari, A. Dvivedi, and P. Kumar, Investigations on the fabrication of a patterned tool by chemical etching, Mater. Manuf. Process., vol. 36, no. 16, pp. 1840–1852, 2021. DOI: 10.1080/10426914.2021.1926491.

[66] B. Sadeghi, P. Cavaliere, C.I. Pruncu, M. Balog, M. Marques de Castro, and R. Chahal, Architectural design of advanced aluminum matrix composites: a review of recent developments, Crit. Rev. Solid State Mater. Sci., vol. 49, no. 1, pp. 1–71, 2024. DOI: 10.1080/10408436.2022.2078277.

[67] R. Mishra, J. Militky, V. Baheti, J. Huang, B. Kale, M. Venkataraman, V. Bele, V. Arumugam, G. Zhu, and Y. Wang, The production, characterization and applications of nanoparticles in the textile industry, Text. Prog., vol. 46, no. 2, pp. 133–226, 2014. DOI: 10.1080/00405167.2014.964474.

[68] P. Mao, C. Liu, G. Favraud, Q. Chen, M. Han, A. Fratalocchi, and S. Zhang, Broadband single molecule SERS detection designed by warped optical spaces, Nat. Commun., vol. 9, no. 1, pp. 5428, 2018. DOI: 10.1038/s41467-018-07869-5.

[69] R. Gao, X. Song, C. Zhan, C. Weng, S. Cheng, K. Guo, N. Ma, H. Chang, Z. Guo, L.-B. Luo, and L. Yu, Light trapping induced flexible wrinkled nanocone SERS substrate for highly sensitive explosive detection, Sens. Actuators, B, vol. 314, pp. 128081, 2020. DOI: 10.1016/j.snb.2020.128081.

[70] J.M. Atkin, S. Berweger, A.C. Jones, and M.B. Raschke, Nano-optical imaging and spectroscopy of order, phases, and domains in complex solids, Adv. Phys., vol. 61, no. 6, pp. 745–842, 2012. DOI: 10.1080/00018732.2012.737982.

[71] Y. Wang, B. Ai, Z. Wang, Y. Guan, G. Xiao, and G. Zhang, Light-trapping perforating microcone arrays for angle-insensitive and broadband SERS, Appl. Surf. Sci., vol. 615, pp. 156271, 2023. DOI: 10.1016/j.apsusc.2022.156271.

[72] N. Van Huong Binh, V.K. Tran, P. Quoc Hoa, N.T. Hoang, and P.H. Tu, Exact solution for free vibration analysis of non-uniform thickness functionally graded porous nanosheet with surface effect based on variable nonlocal and length-scale parameters, Mech. Based Des. Struct. Mach., vol. 53, no. 3, pp. 1635–1667, 2025. DOI: 10.1080/15397734.2024.2390666.

[73] D.C. Mukunda, V.K. Joshi, and K.K. Mahato, Light emitting diodes (LEDs) in fluorescence-based analytical applications: a review, Appl. Spectrosc. Rev., vol. 57, no. 1, pp. 1–38, 2022. DOI: 10.1080/05704928.2020.1835939.

[74] B.-X. Wang, C. Xu, G. Duan, W. Xu, and F. Pi, Review of broadband metamaterial absorbers: from principles, design strategies, and tunable properties to functional applications, Adv. Funct. Materials., vol. 33, no. 14, pp. 2213818, 2023. DOI: 10.1002/adfm.202213818.

[75] V. Dhandapani, B. Raj, Ashima , Design and performance assessment of graded channel gate-all-around silicon nanowire FET for biosensing applications, Silicon, 2023;15(8):3535–3542. DOI: 10.1007/s12633-022-02272-8.

[76] J. Zhang, B. Liu, H. Chen, L. Zhang, and X. Jiang, Application and method of surface plasmon resonance technology in the preparation and characterization of biomedical nanoparticle materials, Int. J. Nanomed., vol. 19, pp. 7049–7069, 2024. DOI: 10.2147/IJN.S468695.

[77] M.Z. Tijjani, J. Deng, J.A. Opeyemi, and A. Aliyu, Exploring bandgap tuning and vibration isolation performance of innovative negative stiffness metastructures, Mech. Adv. Mater. Struct., vol. 32, pp. 1–18, 2025. DOI: 10.1080/15376494.2025.2458777.

[78] X. Zhang, Z. Shao, X. Zhang, Y. He, and J. Jie, Surface charge transfer doping of low-dimensional nanostructures toward high-performance nanodevices, Adv. Mater., vol. 28, no. 47, pp. 10409–10442, 2016. DOI: 10.1002/adma.201601966.

[79] V. Skrypnychuk, G.-J.A.H. Wetzelaer, P.I. Gordiichuk, S.C.B. Mannsfeld, A. Herrmann, M.F. Toney, and D.R. Barbero, Ultrahigh mobility in an organic semiconductor by vertical chain alignment, Adv. Mater., vol. 28, no. 12, pp. 2359–2366, 2016. DOI: 10.1002/adma.201503422.

[80] A. Shoukat, F. Aslam, M. Israr Ur Rehman, Ibrahim , Emerging trends in low band gap perovskite solar cells: materials, device architectures, and performance optimization, Mol. Phys, vol. 122, pp. e2316273(1-27), 2024. DOI: 10.1080/00268976.2024.2316273.

[81] M.G. Villalva, J.R. Gazoli, and E.R. Filho, Comprehensive approach to modeling and simulation of photovoltaic arrays, IEEE Trans. Power Electron., vol. 24, no. 5, pp. 1198–1208, 2009. DOI: 10.1109/TPEL.2009.2013862.

[82] M.P. Henry, and C.K. Ratnayake, Electrochemical properties of columns in capillary electrochromatography: I. Ohm's law, resistivity and field strength, J. Chromatogr. A, vol. 1079, no. 1-2, pp. 69–76, 2005. DOI: 10.1016/j.chroma.2005.02.085.

[83] S.D. Hutagalung, M.M. Fadhali, R.A. Areshi, and F.D. Tan, Optical and electrical characteristics of silicon nanowires prepared by electroless etching., Nanoscale Res. Lett., vol. 12, no. 1, pp. 425, 2017. DOI: 10.1186/s11671-017-2197-3.

[84] C. Li, S. Cao, and T. He, Micro/nano-scale transient thermo-viscoelastic responses for 1D temperature-dependent polymer-based rod heated by the ultra-short pulse laser based on nonlocal single-phase-lag heat conduction and Eringen's differential elasticity, Mech. Adv. Mater. Struct., vol. 31, pp. 1–15, 2024. DOI: 10.1080/15376494.2024.2408638.

[85] H. Karaağaç, E. Peksu, B. Alhalaili, and M. Saif Islam, One-Dimensional Silicon Nano-/Microstructures Based Opto-Electronic Devices. Progress in Nanoscale and Low-Dimensional Materials and Devices: Properties, Synthesis, Characterization, Modelling and Applications, Springer, USA; p. 731–766, 2022.

[86] I. Leontis, M.A. Botzakaki, S.N. Georga, and A.G. Nassiopoulou, Study of Si nanowires produced by metal-assisted chemical etching as a light-trapping material in n-type c-Si solar cells, ACS Omega, vol. 3, no. 9, pp. 10898–10906, 2018. DOI: 10.1021/acsomega.8b01049.

[87] M. Rahmani, S. Amdouni, M-a Zaïbi, and A. Meftah, Effect of etching duration on the morphological and opto-electrical properties of silicon nanowires obtained by Ag-assisted chemical etching, Silicon, vol. 13, no. 1, pp. 179–187, 2021. DOI: 10.1007/s12633-020-00416-2.

[88] A. Lale, A. Grappin, A. Lecestre, L. Mazenq, J. Launay, and P. Temple-Boyer, Top-down integration of suspended N+/P/N + silicon-nanowire-based ion-sensitive field effect transistors for pH analysis at the submicronic scale, Thin Solid Films, vol. 764, pp. 139609, 2023. DOI: 10.1016/j.tsf.2022.139609.

[89] Y. Li, Preparation method and application of silicon nanowires, HSET, vol. 32, pp. 237–244, 2023. DOI: 10.54097/hset.v32i.5172.

[90] J. Fan, and K.A. Alnowibet, Relative frequencies of perovskite solar cells strengthened by composite materials: application of deep neural networks for solving the vibration problem, Mech. Adv. Mater. Struct., vol. 31, no. 27, pp. 9517–9533, 2024. DOI: 10.1080/15376494.2023.2275170.

[91] J. Li, S. Zhang, K.W. Paik, Y.H. Wong, P. He, and S. Zhang, Present status and prospects of nano-silver particles in the electronic field: a review, J. Adhes. Sci. Technol., vol. 39, no. 3, pp. 281–318, 2025. DOI: 10.1080/01694243.2024.2408370.

[92] Y. Liu, H. Wang, H. Qi, F. Qiao, and S. Zhuang, Recent comprehensive review on synthesis, modification, applications, and advanced characterization of TiO2 mesocrystals-based composite materials, Catal. Rev., vol. 66, pp. 1–42, 2024. DOI: 10.1080/01614940.2024.2446475.